Article

Y chromosome loss in cancer drives growth by evasion of adaptive immunity

https://doi.org/10.1038/s41586-023-06234-x

Received: 1 September 2022

Accepted: 18 May 2023

Published online: 21 June 2023

Check for updates

Hany A. Abdel-Hafiz[1,6], Johanna M. Schafer[2,5,6], Xingyu Chen[1,6], Tong Xiao[2], Timothy D. Gauntner[2], Zihai Li[2,7] & Dan Theodorescu[1,3,4,7]✉

Loss of the Y chromosome (LOY) is observed in multiple cancer types, including 10–40% of bladder cancers[1–6], but its clinical and biological significance is unknown. Here, using genomic and transcriptomic studies, we report that LOY correlates with poor prognoses in patients with bladder cancer. We performed in-depth studies of naturally occurring LOY mutant bladder cancer cells as well as those with targeted deletion of Y chromosome by CRISPR–Cas9. Y-positive (Y^+) and Y-negative (Y^-) tumours grew similarly in vitro, whereas Y^- tumours were more aggressive than Y^+ tumours in immune-competent hosts in a T cell-dependent manner. High-dimensional flow cytometric analyses demonstrated that Y^- tumours promote striking dysfunction or exhaustion of $CD8^+$ T cells in the tumour microenvironment. These findings were validated using single-nuclei RNA sequencing and spatial proteomic evaluation of human bladder cancers. Of note, compared with Y^+ tumours, Y^- tumours exhibited an increased response to anti-PD-1 immune checkpoint blockade therapy in both mice and patients with cancer. Together, these results demonstrate that cancer cells with LOY mutations alter T cell function, promoting T cell exhaustion and sensitizing them to PD-1-targeted immunotherapy. This work provides insights into the basic biology of LOY mutation and potential biomarkers for improving cancer immunotherapy.

The Y chromosome is essential for male sex determination and spermatogenesis[7]. Recent studies, aided by advances in sequencing technologies and CRISPR-mediated knockout of the entire Y chromosome[8], have begun to characterize the function of the Y chromosome in a variety of physiological contexts. In ageing men, LOY has been associated with many adverse health consequences. For example, LOY in haematopoietic cells is associated with an increased risk of several diseases, including cardiac fibrosis[9] and multiple cancer types[1–3,10]. In bladder cancer, LOY has been found in 10–40% of tumours[4–6,11–15]. This is unsurprising, since bladder cancer is commonly caused by environmental exposures to tobacco and industrial chemicals, which are known to result in DNA damage and LOY[16–18]. Here we describe how LOY and the corresponding loss of Y chromosome genes such as *KDM5D* and *UTY* confer an aggressive phenotype to bladder cancer, while also making LOY tumours more vulnerable to immunotherapy.

Here we developed Y^+ and Y^- cancer cell models in mice for in vitro and in vivo studies using naturally arising bladder cancer cells with LOY as well as CRISPR-mediated deletion of the entire Y chromosome. We also developed a LOY gene expression signature to interrogate human specimens. We show that cancer cells with LOY have a more aggressive growth phenotype and that low LOY gene signature scores are associated with a poor clinical prognosis for patients with cancer. Using spectral flow cytometry and GeoMX hi-plex spatial proteomic analyses, we showed that mouse tumours with LOY exhibit an immunosuppressive tumour microenvironment (TME) with significant $CD8^+$ T cell exhaustion. We found similar results in human bladder cancer specimens with LOY using single-nuclei RNA sequencing (snRNA-seq) and histology-based analyses using co-detection by indexing (CODEX). The clinical relevance of these findings is further supported by the observation that patients with bladder cancer exhibiting LOY had an improved response to immune checkpoint blockade (ICB) targeting PD-1/PD-L1, which is commonly used to treat advanced bladder cancer[19,20].

Collectively, we provide evidence linking LOY in bladder cancer to more aggressive tumour growth and a poor prognosis. Furthermore, we show that LOY tumours promote $CD8^+$ T cell exhaustion in the TME, predisposing them to a therapeutic vulnerability to ICB in male patients.

LOY is associated with a worse patient outcome

We created a Y chromosome RNA expression signature score based on 18 Y-encoded genes that are expressed in normal bladder urothelium[21] (Extended Data Fig. 1a,b). We used this score to stratify the overall survival of 300 men with locally advanced muscle-invasive bladder cancer (MIBC) in The Cancer Genome Atlas (TCGA) transcriptomic data[22]. The samples were divided into two groups on the basis of average Y chromosome signature scores: Y_{high} ($n = 182$) and Y_{low} ($n = 118$) (Fig. 1a,b). Age (34–90 years), stage (tumour, lymph node or metastatic lesion), race (white, African American or Asian) and tumour grade (high or low) did not differ between Y_{high} and Y_{low} samples (Fig. 1a). However, patients with low Y chromosome gene expression score

[1]Department of Urology, Cedars–Sinai Medical Center, Los Angeles, CA, USA. [2]Pelotonia Institute for Immuno-Oncology, The Ohio State University Comprehensive Cancer Center–The James, Columbus, OH, USA. [3]Department of Pathology and Laboratory Medicine, Cedars-Sinai Medical Center, Los Angeles, CA, USA. [4]Cedars-Sinai Cancer Center, Los Angeles, CA, USA. [5]Present address: Roche Diagnostics Solutions, Oro Valley, AZ, USA. [6]These authors contributed equally: Hany A. Abdel-Hafiz, Johanna M. Schafer, Xingyu Chen. [7]These authors jointly supervised this work: Zihai Li, Dan Theodorescu. ✉e-mail: dan.theodorescu@cshs.org

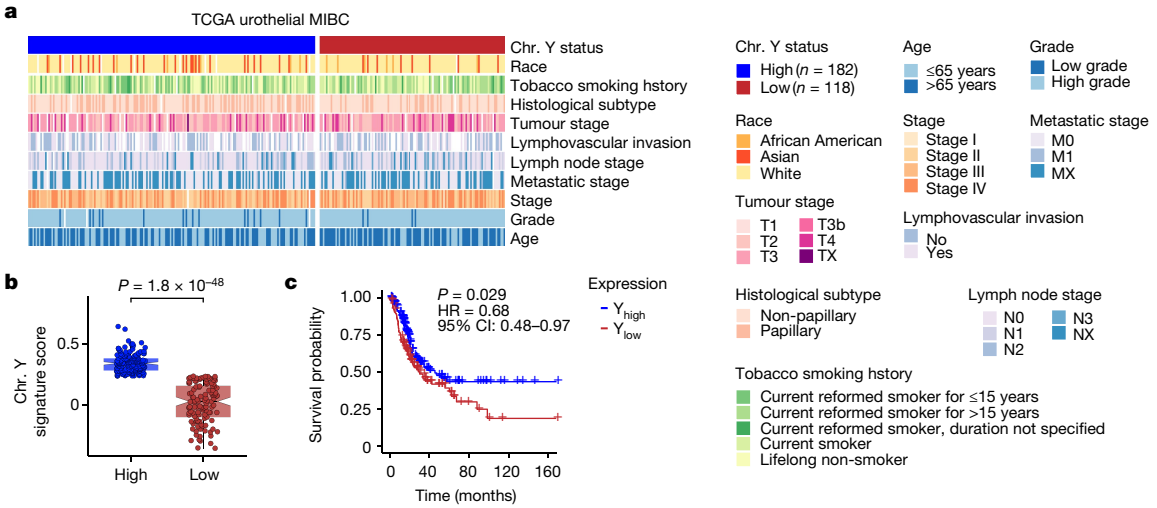

Fig. 1 | LOY is associated with a worse prognosis for men with MIBC. a, Heat map of clinical parameters and metadata for 300 male patients with MIBC from TCGA data. Chr. Y, Y chromosome. **b**,**c**, Plot of Y chromosome gene expression (**b**) and Kaplan–Meier survival curve (**c**) associated with Y_{high} ($n = 182$) and Y_{low} ($n = 118$) samples identified in **a**. CI, confidence interval; HR, hazard ratio. Differences in gene expression and survival were based on Wilcoxon rank-sum test and log-rank statistics, respectively. In box plots, the centre line represents the mean and box edges show first and third quartiles. Minimum and maximum datapoints are included.

had significantly ($P = 0.029$) worse overall survival compared with those with higher expression (Fig. 1c). Notably, decreased individual expression of four Y chromosome genes (*KDM5D*, *UTY* (also known as *KDM6C*), *TBL1Y* and *ZFY*) was also associated with a poor prognosis (Extended Data Fig. 1c). Similar results for survival were found when 834 patients with non-muscle-invasive bladder cancer (NMIBC) were evaluated[23] (Extended Data Fig. 1d), suggesting that LOY is present early in disease progression.

To confirm the robustness of the results obtained with our Y chromosome signature score, we also carried out virtual karyotyping analyses using two different methods. In the first study, we used TCGA RNA data to show that extreme downregulation of chromosome Y (EDY) increased cancer risk in 12 cancer types, including bladder cancer[1]. In the second study, we used TCGA DNA sequencing data and mosaic alteration detection for LOY (MADLOY) to detect LOY from genotype array intensity data[24]. These two studies validated our Y chromosome signature, as Y_{low} tumour specimens were also identified as having EDY and LOY by these techniques, and suggest that low expression of Y chromosome genes is due to the loss of the Y chromosome (Extended Data Fig. 1e).

Development of LOY mouse bladder cancer models

To determine why Y_{low} bladder cancer is more aggressive than Y_{high} tumours, we assessed Y chromosome gene expression in MB49, a well-studied mouse bladder cancer cell line that has been shown to naturally lose the Y chromosome[25–27]. We selected and expanded single-cell clones from the heterogeneous MB49 parental population and assessed the expression of seven genes located on the male-specific region on chromosome Y that are commonly expressed in both mouse and human bladder cells[21]. Only three (*Kdm5d*, *Uty* and *Ddx3y*) out of the seven genes were expressed in the MB49 line (Extended Data Fig. 2a and Supplementary Table 1). We also evaluated *Eif2s3y* expression, as it is an additional mouse Y chromosome gene that is expressed in urothelium[21]. We pooled 16 clones that exhibited no Y chromosome gene expression compared to positive controls (normal mouse testis and the parental MB49 line) to create a polyclonal Y^- cell line. The female bladder cell line NA13 (ref. 28) and the breast cancer line E0771 (ref. 29) served as negative controls. Similarly, we pooled together 16 clones that expressed the four Y chromosome genes at similar levels to positive controls to create a polyclonal Y^+ cell line (Extended Data Fig. 2b,c). Next, using whole-exome sequencing (WES), we confirmed that the lack of Y chromosome gene expression in the MB49 sublines was due to LOY (Extended Data Fig. 2d).

Effect of LOY on cancer growth

We observed no differences in proliferation between the Y^- and Y^+ sublines in 2D or 3D in vitro culture (Fig. 2a and Extended Data Fig. 3a,b). To investigate the effect of LOY on tumour growth in vivo, we injected the Y^- and Y^+ lines subcutaneously into immune-competent wild-type male C57BL/6 mice. We found that Y^- tumours exhibited an approximately twofold increased tumour growth rate compared with Y^+ tumours (Fig. 2b). This observation provided compelling clinical relevance for our model system, since it paralleled the relationship observed in human tumours. We then assessed the contribution of host immunity to the differential growth by injecting each cell type into wild-type and *Rag2*$^{-/-}$*Il2rg*$^{-/-}$ (deficient in T cells, B cells and natural killer cells) male mice. Again, Y^- tumours grew significantly faster than Y^+ tumours in the wild-type mice, whereas both cell types grew at the same rate in the immunocompromised *Rag2*$^{-/-}$*Il2rg*$^{-/-}$ mice (Fig. 2c), indicating that the Y^- tumours were more efficient in evading anti-tumour adaptive immunity.

To separate Y chromosome loss from other potential differences in genetic background between the Y^+ and Y^- lines, we deleted the Y chromosome from Y^+ cells using CRISPR–Cas9-mediated chromosome depletion using previously established techniques[8,9] (Fig. 2d). Depletion of the Y chromosome alone (CRISPR Y-KO) promoted faster tumour growth compared with the scrambled guide RNA Y^+ control (CRISPR Y-Scr) MB49 cells in immune-competent mice (Fig. 2e and Extended Data Fig. 3b,c). This essentially reproduced the findings from naturally occurring Y^- bladder cancer cells.

We next aimed to define the molecular drivers in Y^- tumours that contribute to immune evasion. Of the three genes shared between humans and MB49 cells, low expression of *KDM5D* and *UTY* were the only human genes whose loss of expression was associated with an unfavourable prognosis in human bladder cancer (Fig. 2f,g, Extended Data Fig. 1c and Supplementary Table 1). We therefore engineered Y^+ and Y^- sublines in which *Uty* or *Kdm5d* was either knocked out or overexpressed. We found that Y^+ tumours in which *Uty* or *Kdm5d* was knocked out exhibited an

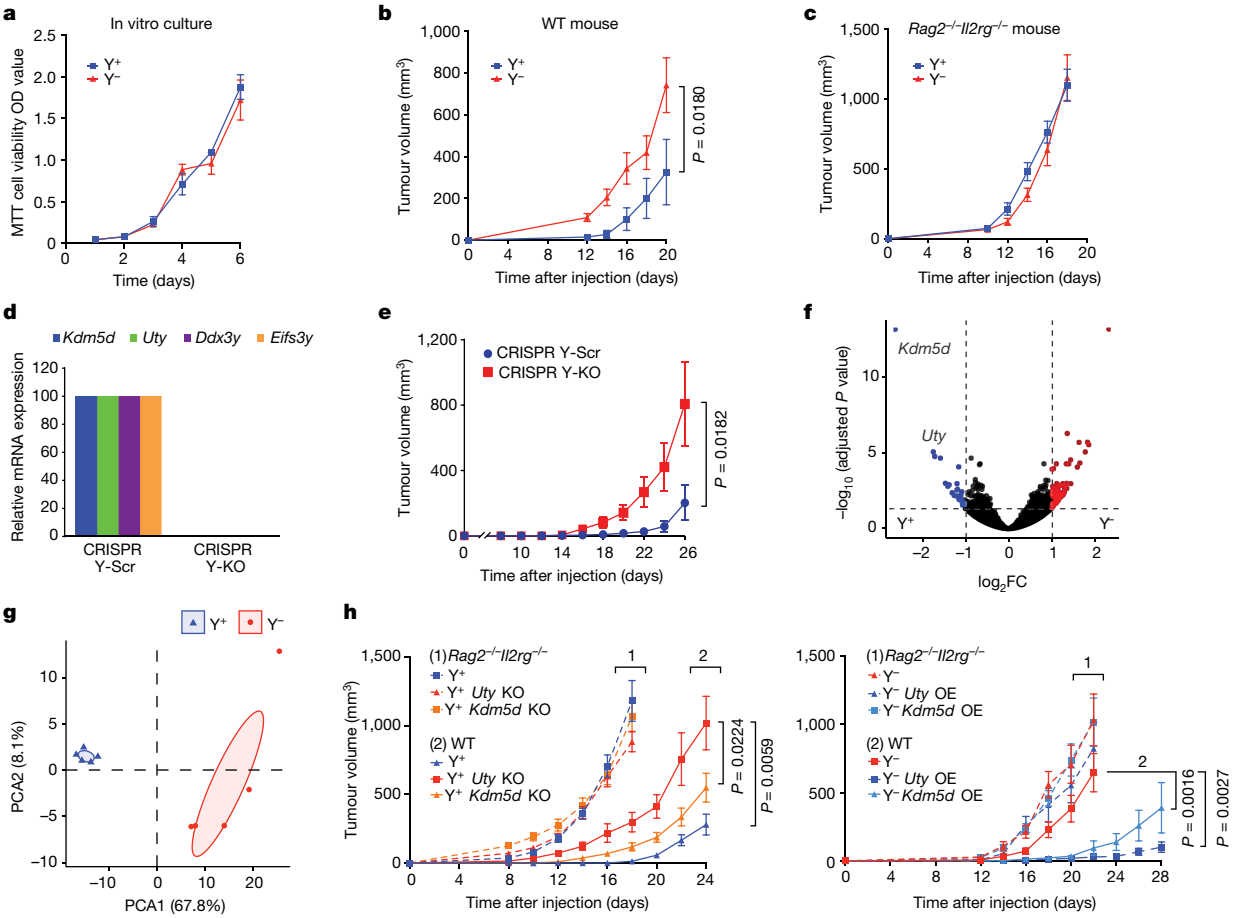

Fig. 2 | LOY and deletion of the Y chromosome genes *Kdm5d* and *Uty* promotes bladder tumour growth in an immune-competent host. **a**, Proliferation of Y$^+$ and Y$^-$ MB49 cells in vitro (by MTT cell viability assay) over a six-day time course. Data are mean ± s.e.m. $n = 3$ biological replicates. OD, optical density. **b**,**c**, Tumour volume of Y$^+$ and Y$^-$ MB49 cells grown subcutaneously in wild-type (WT) C57BL/6 (**b**; $n = 10$ mice per group) or *Rag2*$^{-/-}$*Il2rg*$^{-/-}$ (**c**; $n = 10$ mice per group) male mice. **d**, Relative mRNA expression (determined by RT–qPCR) of *Uty*, *Kdm5d*, *Eifs3y* and *Ddx3y* in CRISPR-generated Y-Scr and Y-KO MB49 lines. **e**, Tumour volume of CRISPR Y-Scr and CRISPR Y-KO MB49 cells grown subcutaneously in wild-type C57BL/6 male mice ($n = 10$ (Y-Scr) and 8 (Y-KO) mice per group). **f**, Volcano plot of statistically significant (Benjamini–Hochberg method, $P < 0.05$) differentially expressed genes (DEGs) from Y$^+$ (blue) and Y$^-$ (red) MB49 cells that exhibit a positive or negative $\log_2$ fold difference in expression of greater than one. FC, fold change. **g**, PCA of Y$^+$ (blue) and Y$^-$ (red) DEGs described in **f**. Shaded areas encompass regions where the principal component falls within a 95% confidence internal. **h**, Left, tumour volume of Y$^+$ *Uty*-KO and Y$^+$ *Kdm5d*-KO cell lines injected subcutaneously into wild-type ($n = 10$ mice per group) or *Rag2*$^{-/-}$*Il2rg*$^{-/-}$ ($n = 10$ mice per group) male mice. Right, similarly, Y$^-$, *Uty*-overexpression (OE) and *Kdm5d*-OE cell lines were implanted into wild-type ($n = 10$ mice per group) or *Rag2*$^{-/-}$*Il2rg*$^{-/-}$ ($n = 8$, 6 and 6 mice per group, respectively) male mice. All mouse experiments are representative of two independent experiments. Repeated measures two-way ANOVA; comparisons were made with the Y$^+$ and Y$^-$ controls in **h**. Data are mean ± s.e.m.

increased growth rate compared with Y$^+$ tumours in wild-type hosts, but no such difference was observed in *Rag2*$^{-/-}$*Il2rg*$^{-/-}$ mice (Fig. 2h). Consistent with these results, overexpression of either *Uty* or *Kdm5d* in Y$^-$ tumours resulted in decreased tumour growth in wild-type mice but not in *Rag2*$^{-/-}$*Il2rg*$^{-/-}$ mice (Fig. 2h). Again, all lines shared the same growth kinetics in vitro (Extended Data Fig. 3b). Together, these results demonstrate that *Uty* and *Kdm5d* contribute—at least in part—to the impaired anti-tumour immunity of Y$^-$ tumours. Further, identification of *KDM5D* or *UTY* loss in human tumours has the potential to be a useful prognostic factor in determining the clinical aggressiveness of bladder cancer.

LOY cancer cells create an immunosuppressive TME

To further determine the immunological basis of the differential growth of Y$^-$ and Y$^+$ tumours, we sequenced the entire transcriptome from Y$^-$ and Y$^+$ MB49 tumours grown in wild-type mice. We detected 958 DEGs (Extended Data Fig. 4a). Tumours from each genotype were separated by principal component analysis (PCA) (Extended Data Fig. 4b), supporting a distinct molecular architecture. Gene set enrichment analyses (GSEA) performed on DEGs revealed that Y$^+$ tumours were associated with enhanced immune responses compared with Y$^-$ tumours (positive regulation of lymphocyte proliferation: normalized enrichment score (NES) = 1.59, adjusted *P* value = 0.01; lymphocyte mediated immunity: NES = 1.76, adjusted *P* value = 0.01; response to IFNγ: NES = 1.87, adjusted *P* value = 0.01; positive regulation of T cell activation: NES = 1.80, adjusted *P* value = 0.01) (Extended Data Fig. 4c). We then further genetically defined the roles of T cells and B cells using mice with deficiency in each cellular compartment. We observed similar enhanced growth of Y$^-$ tumours in wild-type as well as in B cell-deficient *Ighm*-knockout (KO) mice (Fig. 3a). However, the differential growth of Y$^+$ and Y$^-$ tumours was eliminated in *Rag2*$^{-/-}$ and *Tcrb*$^{-/-}$*Tcrd*$^{-/-}$ mice, confirming that the increased tumour growth control of Y$^+$ tumours was due to endogenous anti-tumour T cell immunity (Fig. 3a).

We next used high-dimensional spectral flow cytometry to delineate the difference in intratumoural CD45$^+$ immune cell populations between Y$^+$ and Y$^-$ tumours. Y$^-$ tumours were enriched in the proportion of total CD8$^+$ T cells (Fig. 3b–e, Extended Data Fig. 5a–c and

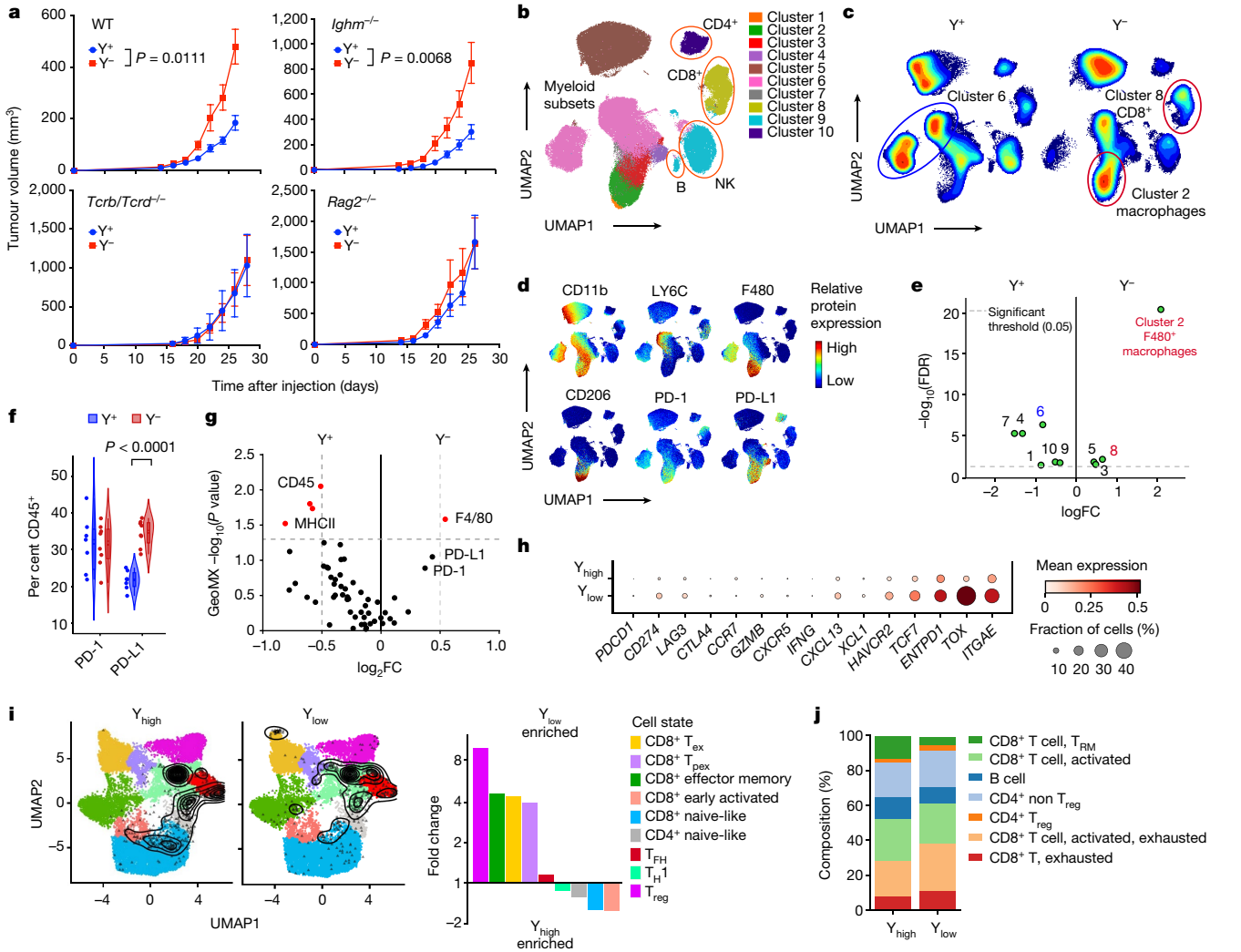

Fig. 3 | Y_{low} bladder cancer overcomes T cell immunity and endows an immune-suppressive TME. a, Tumour growth curves of Y^+ and Y^- MB49 cells grown subcutaneously in wild-type ($n = 8$ mice per group), *Ighm*$^{-/-}$ ($n = 10$ (Y^+) and 7 (Y^-) mice per group), *Tcrb*$^{-/-}$/*Tcrd*$^{-/-}$ ($n = 8$ (Y^+) and 9 (Y^-) mice per group) or *Rag2*$^{-/-}$ ($n = 8$ (Y^+) and 10 (Y^-) mice per group) male mice. Data are representative of two independent experiments. Statistical significance was determined by repeated measures two-way ANOVA. Data are mean ± s.e.m. **b**, Uniform manifold approximation and projection for dimension reduction (UMAP) of spectral flow cytometry analysis of CD45$^+$ immune cell subsets from Y^+ and Y^- MB49 tumours. NK, natural killer cells. **c**,**d**, Heat map of UMAP immune cell populations (**c**) and individual protein markers (**d**) from Y^+ and Y^- MB49 tumour-infiltrating lymphocytes detailed in **b**. **e**, Volcano plot of significantly different ($P < 0.05$, green) UMAP clusters between Y^+ and Y^- MB49 tumours. Red and blue labels (and circles in **c**) denote Y^- and Y^+-associated clusters of interest, respectively. FDR, false discovery rate. **f**, Violin plot of PD-1 and PD-L1 expression in Y^- and Y^+ MB49 CD45$^+$ immune cells. Two-sided unpaired *t*-test. **g**, Volcano plot of statistically significant (red) GeoMX marker expression between Y^+ and Y^- MB49 tumours. **h**, Dot plot of mean gene expression (checkpoint molecules and markers of T cell activation and exhaustion) and fraction of CD45$^+$ cells from human MIBCs by snRNA-seq. **i**, Left, contour plot of T cells from human MIBC snRNA-seq overlaid onto an annotated UMAP as described in Methods. Right, fold change enrichment between Y_{low} and Y_{high} MIBC T cell subsets. T_{ex}, exhausted T cell; T_{FH}, T follicular helper cell; T_H1, T helper 1 cell; T_{pex}, progenitor exhausted T cell; T_{reg}, T regulatory cell. **j**, Stacked bar graph of immune cell subsets and T cell differentiation states from CODEX-stained Y_{low} and Y_{high} human MIBC tissue sections. T_{RM}, resident memory T cell.

Supplementary Fig. 1) as well as immunosuppressive (CD11b$^+$F4/80$^+$LY6C$^-$CD206$^+$) macrophages. Tumour-infiltrating macrophages in Y^+ tumours had a more inflammatory (CD11b$^+$F4/80$^+$LY6C$^+$CD206$^-$) phenotype (Fig. 3b–e and Extended Data Fig. 5a–c). Of note, the percentage of PD-L1$^+$CD45$^+$ immune cells (Fig. 3f) and PD-L1 expression levels (Extended Data Fig. 5d) were increased in Y^- tumours. We observed similar results in CRISPR Y-Scr and CRISPR Y-KO MB49 tumours, in that the CRISPR Y-KO tumours contained a greater proportion of CD8$^+$ T cells as well as immunosuppressive CD206$^+$PD-L1$^+$ macrophages (Extended Data Fig. 5e,f). Consistent with these findings, increased numbers of F4/80$^+$ macrophages and increased PD-1/PD-L1 expression were also observed histologically in Y^- MB49 tissue sections using GeoMX hi-plex spatial proteomic analysis (Fig. 3g and Extended Data Fig. 6a–c).

To determine whether the TME of Y^- mouse tumours reflects the clinical data, we deconvoluted RNA-sequencing (RNA-seq) data from urothelial bladder cancer in the TCGA database and mined a previously published MIBC snRNA-seq dataset[30]. Similar to our comparisons of Y^- and Y^+ MB49 cells, CD8$^+$ T cells in Y_{low} tumours exhibited increased expression of immune checkpoint molecules such as *CD274* (which encodes PD-L1), *LAG3* and *HAVCR2* (which encodes TIM3), as well as markers for both progenitor T cells (*TCF7*) and terminal exhausted T cells (*TOX*) (Fig. 3h). We then compared the proportions of these T cell subsets between tumour types by overlaying each cell sequenced with an annotated reference UMAP[31]. Y_{low} bladder cancers contained a higher proportion of exhausted and progenitor exhausted CD8$^+$ T cells, as well as T regulatory cells (Fig. 3i).

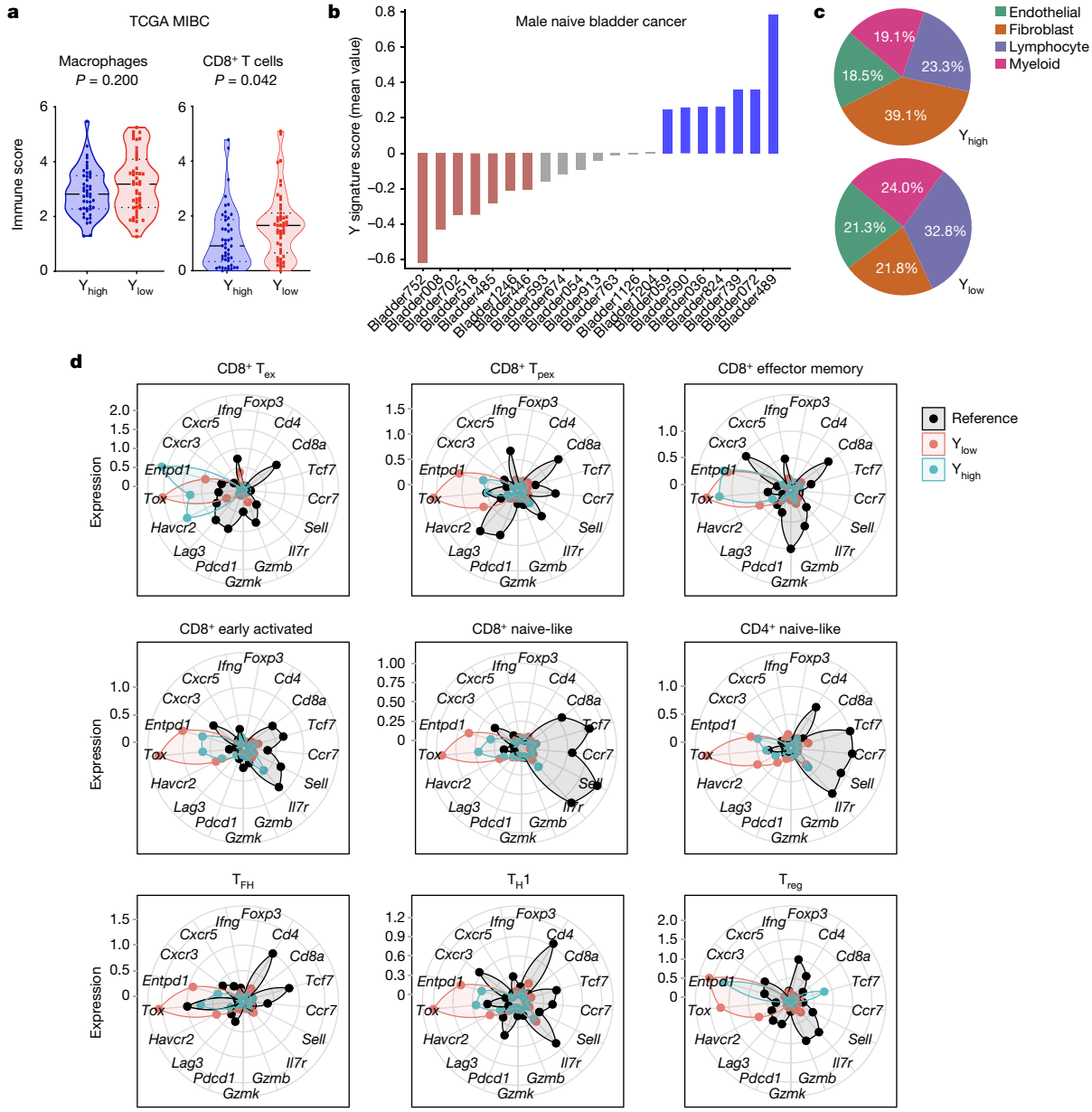

Fig. 4 | Human Y_{low} bladder cancers are enriched with $CD8^+$ T cells with evidence of exhaustion. a, Violin plots of macrophages and $CD8^+$ T cell immune scores from Y_{high} and Y_{low} bladder cancer using urothelial bladder cancer TCGA data ($n = 47$ per group) and the microenvironment cell populations (MCP) counter method. Two-sided Wilcoxon rank-sum test. **b**, Y signature score using snRNA-seq data across 21 male naive bladder cancers. Colours denote Y_{high} (blue; >0.2 mean Y signature score), Y_{low} (red; <0.2 mean Y signature score) and $Y_{intermediate}$ (grey; −0.2 to 0.2 mean Y signature score) patient samples. **c**, Distribution of the indicated non-epithelial immune cell types from samples described in **b**. **d**, Normalized expression of the indicated genes per T cell subtype from MIBC samples identified in **b**. T cells from melanoma and colon cancer samples were used to generate the reference T cell subtypes and gene expression.

To further validate the snRNA-seq results and to assess levels of T cell exhaustion histologically, we evaluated immune-focused CODEX results from patient-matched samples[30]. Consistent with our spectral flow cytometry and snRNA-seq analyses, Y_{low} bladder cancers contained a higher proportion of dysfunctional $CD8^+$ T cells (Fig. 3j). Of note, higher proportions of $CD8^+$ T cells were present in Y_{low} than in Y_{high} bladder cancer samples (Fig. 4a–c), but *TOX* expression was found to be higher in all intratumoural T cell subsets of Y_{low} tumours, including $CD8^+$ T cells (naive-like, early activated, exhausted, progenitor exhausted and effector memory) and $CD4^+$ T cells (T regulatory, naive-like, T follicular helper and T helper 1 cells) (Fig. 4d). Together, the data support the notion of LOY tumours promoting $CD8^+$ T cell exhaustion in the TME.

Response of LOY tumours to anti-PD-1/PD-L1

Given that an increase in exhausted and progenitor exhausted $CD8^+$ T cells in the TME is associated with an improved response to anti-PD-1/PD-L1 ICB[32], we treated the Y^+ and Y^- MB49 lines, and the CRISPR Y-Scr and CRISPR Y-KO MB49 lines, with anti-PD-1 blocking antibodies. At the end of the course of treatment, we performed spectral flow cytometry to examine the dynamics of tumour-infiltrating $CD8^+$ T cells with and without ICB[33]. Both clonally selected and CRISPR-generated Y^- tumour models demonstrated an improved response to anti-PD-1 treatment compared with Y^+ tumours (Fig. 5a). Consistent with our analyses of human snRNA-seq data (Fig. 3h,i), $CD8^+$ T cells from isotype control antibody-treated Y^- tumours showed increased expression of

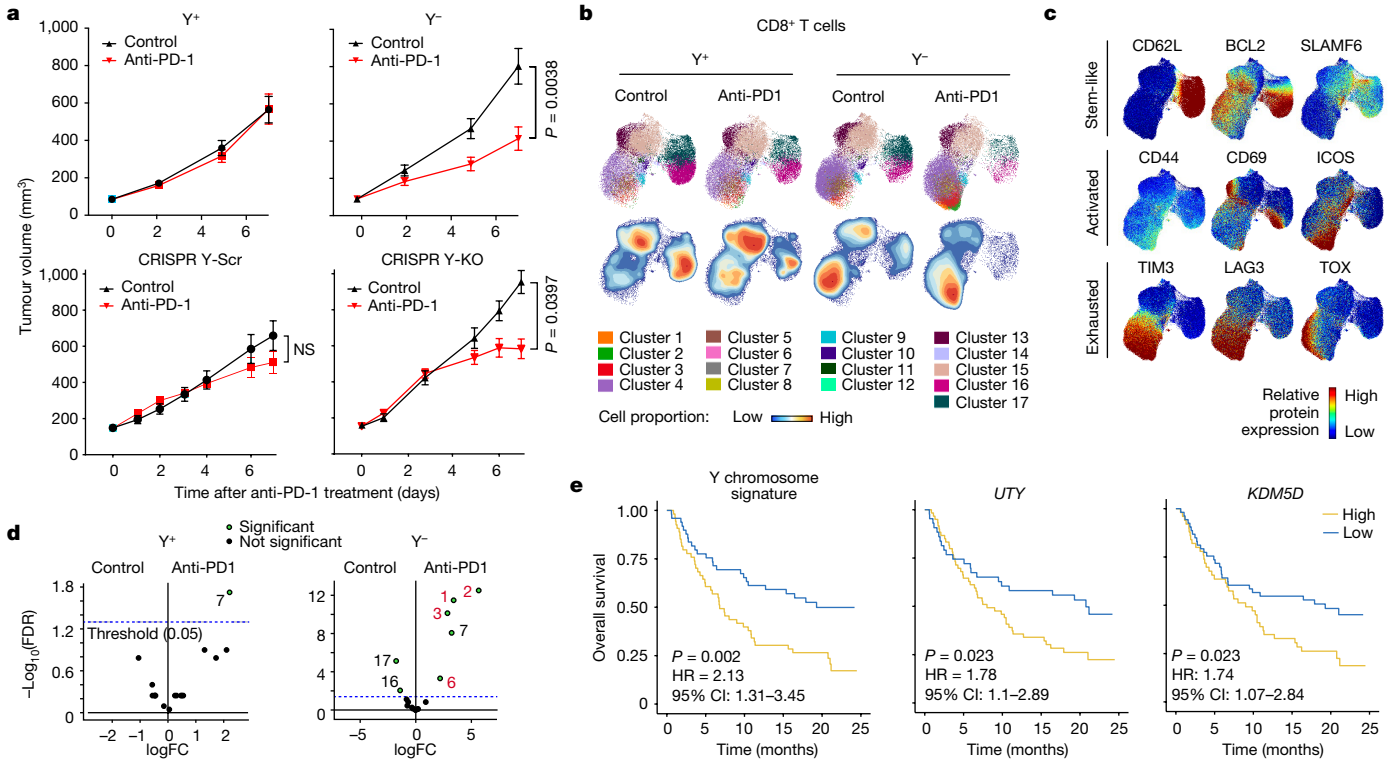

Fig. 5 | Improved response of Y_{low} bladder cancer to anti-PD-1 ICB therapy. **a**, Tumour growth curves of Y^+ and Y^- (top) and CRISPR Y-Scr and CRISPR Y-KO (bottom) treated with 200 µg anti-PD-1 antibody or isotype control IgG. Y^+ isotype: $n = 17$ mice; Y^+ anti-PD-1: $n = 17$ mice; Y^- isotype: $n = 14$ mice; Y^- anti-PD-1: $n = 16$ mice. Data representative of two independent experiments. CRISPR Y-Scr isotype: $n = 11$ mice; CRISPR Y-Scr anti-PD-1: $n = 11$ mice; CRISPR Y-KO isotype: $n = 15$ mice; CRISPR Y-KO anti-PD-1: $n = 15$ mice. Repeated measures two-way ANOVA. Data are mean ± s.e.m. NS, not significant. **b**, UMAPs of $CD8^+$ T cell spectral flow cytometry results from Y^+ and Y^- MB49 tumours seven days after treatments described in **a**. The UMAPs report cluster analyses (top) and cell proportions (bottom). **c**, UMAP heat maps of individual protein markers for stem-like, activated and exhausted T cells superimposed on the UMAPs in **b**. **d**, Volcano plot of statistically significant (green) UMAP clusters between isotype and anti-PD-1-treated Y^+ and Y^- MB49 tumours. **e**, Left, Kaplan–Meier curves for patients with Y_{high} and Y_{low} bladder cancer treated with anti-PD-L1, from the IMvigor210 dataset. Kaplan–Meier curves for patients with bladder cancer stratified by expression of *UTY* (centre) and *KDM5D* (right). Survival differences are based on log-rank statistics.

exhaustion markers such as TOX and TIM3 compared with Y^+ tumours (Fig. 5b–d and Extended Data Fig. 7a). Notably, $CD8^+$ T cells from Y^- tumours exhibited a greater phenotypic response to anti-PD-1 treatment (Fig. 5d and Extended Data Fig. 7b,c)—from a more exhausted (expressing TIM3, LAG3 and TOX) to a more activated (expressing CD44, ICOS but not TOX) differentiation state (Fig. 5b,c and Extended Data Fig. 7d–f). The less aggressive nature of Y^+ tumours is most apparent at earlier stages of tumour growth (Fig. 2b,e), which we attribute to a more activated lymphocytic cell state at baseline. This can be seen at both the RNA (Extended Data Fig. 4) and protein (Extended Data Fig. 7d,f) level, and is probably the reason that these tumours do not respond as well to anti-PD-1 treatment.

To determine the human relevance of our preclinical work, we evaluated the overall survival of Y_{low} and Y_{high} patients with bladder cancer from the IMvigor210 atezolizumab (anti-PD-L1) clinical trial[34]. Consistent with an improved response of Y^- MB49 tumours to anti-PD-1 treatment, Y_{low} patients with bladder cancer had better outcomes after anti-PD-L1 treatment (Fig. 5e). Similar outcomes were observed if patients were stratified on the basis of *UTY* or *KDM5D* expression, underscoring the important role of these two genes in conferring the LOY phenotype (Fig. 5e). Similar to observations in our mouse models (Fig. 3f and Extended Data Fig. 5d) and evaluations of human bladder cancer specimens (Fig. 3h), PD-L1 levels were enriched in Y_{low} bladder cancer from the IMvigor210 trial (Fig. 6a,b).

Of relevance, a recent report demonstrated that LOY and loss of *KDM5D* induced increased genomic instability in haematopoietic stem and progenitor cells[35]. We therefore evaluated the activation of DNA replication and repair pathways in different tumour types. The expression of markers associated with pathways including DNA damage repair (DDR), mismatch repair and nucleotide excision repair were higher in Y_{low} tumours (Fig. 6c,d), indicating that these tumours were indeed more genomically unstable. Further genetic evaluations of Y_{low} and Y_{high} bladder cancer from this cohort revealed an increase in tumour neoantigen burden (TNB) in Y_{low} tumours that probably contributed to their increased responses to ICB (Fig. 6a,c).

Aside from an increase in TNB, we observed an increased DDR pathway activation in the Y_{low} TCGA tumours (Extended Data Fig. 8a–c) and in the Y^- MB49 cell line (Extended Data Figs. 9 and 10). Together, these results demonstrate that LOY in bladder tumour cells contributes to the aggressive nature of Y_{low} bladder cancer, which can be attributed to effective evasion of T cell immunity secondary to an increased presence of PD-L1-expressing macrophages and ensuing $CD8^+$ T cell exhaustion. Consistent with LOY tumours promoting $CD8^+$ T cell exhaustion in the TME, we found Y^- tumours to be more responsive to anti-PD-1 ICB, underscoring the translational significance of our findings.

Discussion

EDY is a male-specific signature of cancer susceptibility that is strongly linked to LOY and Y chromosome methylation patterns[1]. Given that bladder cancer is the fourth most common cancer in men and that LOY occurs in up to 40% of cases of bladder cancer, regardless of grade and stage[36], the understanding of how LOY contributes to the poor prognoses for bladder cancer in men is an unmet medical need and a

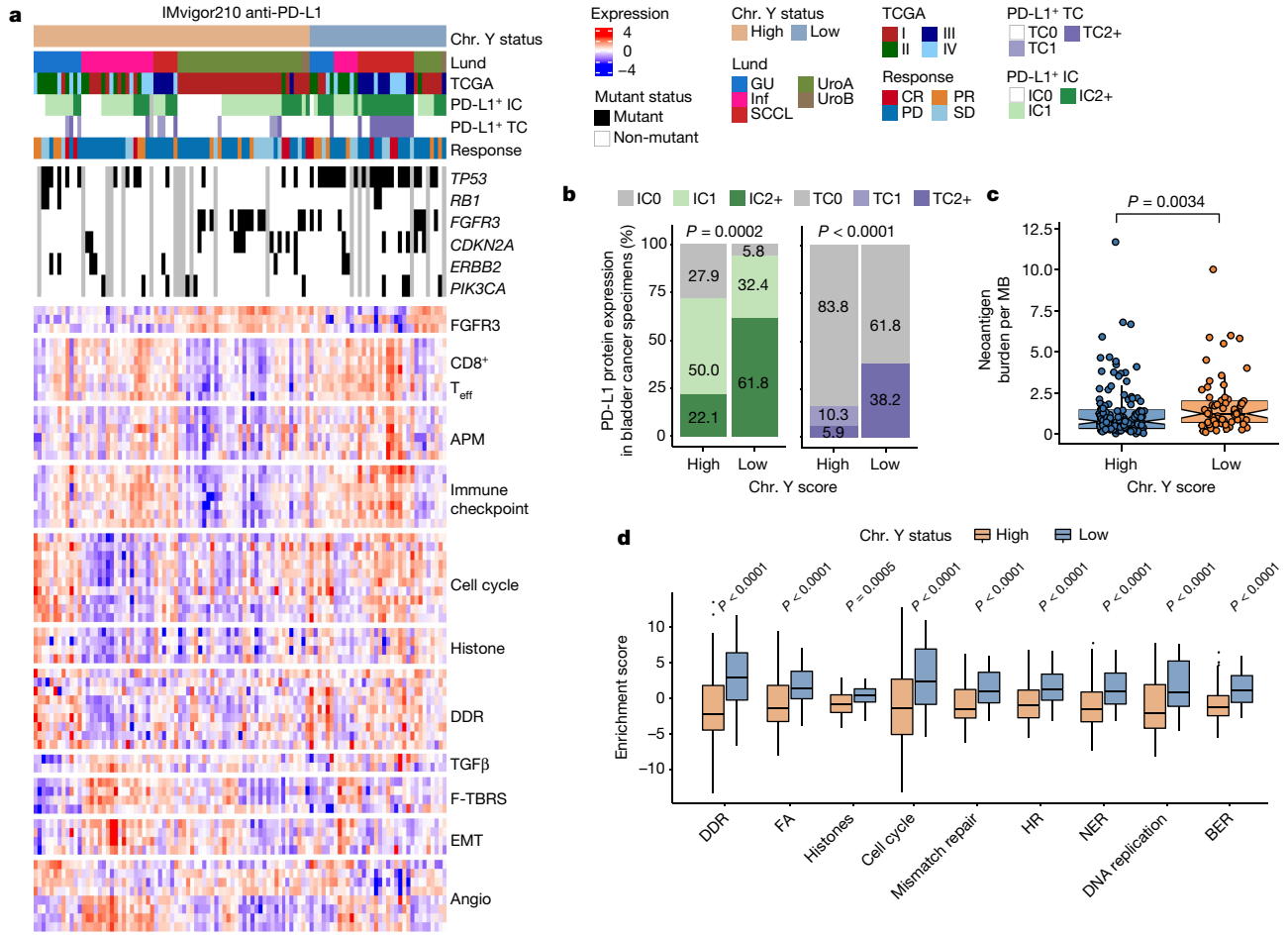

Fig. 6 | Increased genomic instability in Y_{low} bladder cancer. a, Heat map of the indicated pathways and associated metadata from the IMvigor210 anti-PD-L1 clinical trial. Angio, angiogenesis; APM, antigen-processing machinery; CR, complete response; EMT, epithelial-to-mesenchymal transition; F-TBRS, fibroblast TGFβ response signature; GU, genomically unstable; IC, immune cells; Inf, infiltrated; PD, progressive disease; PR, partial response; SCCL, squamous cell carcinoma-like; SD, stable disease; TC, tumour cells; T_{eff}, T effector cells; UroA, urothelial-like A; UroB, urothelial-like B. PD-L1 immunohistochemistry scores: IC0 (<1%), IC1 (≥1% and <5%) or IC2+ (≥5%). **b**, Stacked bar graph of PD-L1 expression in immune cells (left) and tumour cells (right) from Y_{high} and Y_{low} bladder cancer samples identified in **a**. Pearson's Chi-squared test. **c**, Box plot showing neoantigen burden per megabase in Y_{low} ($n = 67$) and Y_{high} ($n = 129$) tumours. Wilcoxon rank-sum test. **d**, Genomic instability pathway enrichment scores from bladder cancer described in **a**. Wilcoxon rank-sum test (Y_{low}: $n = 33$; Y_{high}: $n = 82$). BER, base excision repair; FA, Fanconi anaemia; HR, homologous recombination; NER, nucleotide excision repair. In box plots, the centre line represents the mean and box edges show first and third quartiles. Minimum and maximum datapoints are included.

major biological question. Here we show that the aggressive behaviour of LOY bladder cancer is a consequence of T cell dysfunction. We report increased tumour-associated macrophages, high levels of immune checkpoint molecules and $CD8^+$ T cell exhaustion in Y_{low} tumours. Consistent with known mechanisms of response to immunotherapy[32], patients with Y_{low} tumours exhibit an improved response to anti-PD-1/PD-L1 ICB.

We first examined TCGA RNA-seq data for bladder cancer using a Y chromosome gene expression signature, finding that patients with LOY had a reduced overall survival following surgery. Given that the MB49 mouse bladder cancer model is widely used to investigate different aspects of bladder cancer biology and has previously been shown to lose the Y chromosome[37], we used MB49 to isolate two distinct, naturally arising cell populations to represent Y_{low} and Y_{high} tumours. Consistent with the human data, MB49 tumours with LOY grew more aggressively. Similar results were seen when knocking out *UTY* and *KDM5D*, two chromatin-modifying genes located on the Y chromosome. Overexpressing these genes in Y^- cell lines rescued tumour control in the immune-competent host. Loss of *UTY*, the male counterpart of *UTX* (*KDM6A*) located on the X chromosome, has been reported to promote bladder cancer development[36,38]. Unlike UTX, UTY possesses very low demethylase activity for H3K27[39], suggesting that UTY suppresses bladder cancer development in a demethylase-independent manner. By contrast, KDM5D negatively regulates the expression of genes involved in tumour cell invasion, such as matrix metalloproteinase family genes, by demethylation of their H3K4me3 marks. Downregulation of *KDM5D* expression increases H3K4me3 levels at target gene promoter regions, leading to a more aggressive phenotype and the development of metastasis[40].

Using mouse models lacking T cells (*Tcrb*$^{-/-}$*Tcrd*$^{-/-}$), B cells (*Ighm*$^{-/-}$) or both T cells and B cells (*Rag2*$^{-/-}$*Il2rg*$^{-/-}$ or *Rag2*$^{-/-}$), we demonstrated that the differential growth observed between Y^- and Y^+ MB49 tumours was T cell-dependent. Multispectral flow cytometric analysis of these tumours and in-depth analyses of human MIBC specimens using snRNA-seq and histological applications revealed that $CD8^+$ T cells within the Y^+ tumours retained their anti-tumour immunity, whereas $CD8^+$ T cells in Y^- tumours were phenotypically exhausted. Of note, the expression of TOX—a transcription factor typically known to transcriptionally and epigenetically programme $CD8^+$ T cells towards terminal exhaustion[41,42]—was increased in $CD8^+$ and $CD4^+$ T cells in various differentiation states within Y_{low} bladder cancer specimens. The molecular mechanism of this effect is unclear. In particular, how the loss of Y

chromosome genes from tumour cells leads to upregulation of TOX in tumour-infiltrating T cells and its role in bladder cancer progression warrants further investigation.

Our findings with LOY cancer variants were completely recapitulated with CRISPR–Cas9-mediated chromosome depletion of Y^+ cells, a strong indication that the promotion of $CD8^+$ T cell exhaustion in the TME by LOY tumours was driven entirely by the loss of the Y chromosome, and not by any cryptic clonal variations. In essence, we found that LOY tumours were able to evade adaptive immunity by promoting $CD8^+$ T cell exhaustion. In so doing, LOY tumours were also more responsive to anti-PD-1 ICB because the primary mode of ICB is driving T cell differentiation from exhaustion to effector function. Thus, evaluation of Y chromosome gene expression—and in particular, *UTY* and *KDM5D*—could be used to select patients with bladder cancer for ICB therapy with the expectation of improved response and better survival outcomes. More speculatively, transient pharmacologic inhibition of *UTY* and *KDM5D* may offer enhanced therapeutic benefits for patients with Y_{high} tumours who are undergoing ICB therapy. Future studies will be required to understand the mechanism of LOY-driven tumour evasion and to specifically define the molecular circuitry that connects the loss of *UTY* and/or *KDM5D* to $CD8^+$ T cell exhaustion in the TME. Since age-related LOY is widespread in lymphocytes[43], it will also be of benefit to investigate its effect on immune surveillance. We postulate that early LOY in tumour evolution is an adaptive strategy by tumour cells to evade immunity, with deep biological and therapeutical implications.

Online content

Any methods, additional references, Nature Portfolio reporting summaries, source data, extended data, supplementary information, acknowledgements, peer review information; details of author contributions and competing interests; and statements of data and code availability are available at https://doi.org/10.1038/s41586-023-06234-x.

1. Caceres, A., Jene, A., Esko, T., Perez-Jurado, L. A. & Gonzalez, J. R. Extreme downregulation of chromosome Y and cancer risk in men. *J. Natl Cancer Inst.* **112**, 913–920 (2020).
2. Kido, T. & Lau, Y. F. Roles of the Y chromosome genes in human cancers. *Asian J. Androl.* **17**, 373–380 (2015).
3. Brown, D. W. & Machiela, M. J. Why Y? Downregulation of chromosome Y genes potentially contributes to elevated cancer risk. *J. Natl Cancer Inst.* **112**, 871–872 (2020).
4. Panani, A. D. & Roussos, C. Sex chromosome abnormalities in bladder cancer: Y polysomies are linked to PT1-grade III transitional cell carcinoma. *Anticancer Res.* **26**, 319–323 (2006).
5. Sauter, G. et al. Y chromosome loss detected by FISH in bladder cancer. *Cancer Genet. Cytogenet.* **82**, 163–169 (1995).
6. Powell, I., Tyrkus, M. & Kleer, E. Apparent correlation of sex chromosome loss and disease course in urothelial cancer. *Cancer Genet. Cytogenet.* **50**, 97–101 (1990).
7. Maan, A. A. et al. The Y chromosome: a blueprint for men's health? *Eur. J. Hum. Genet.* **25**, 1181–1188 (2017).
8. Adikusuma, F., Williams, N., Grutzner, F., Hughes, J. & Thomas, P. Targeted deletion of an entire chromosome using CRISPR/Cas9. *Mol. Ther.* **25**, 1736–1738 (2017).
9. Sano, S. et al. Hematopoietic loss of Y chromosome leads to cardiac fibrosis and heart failure mortality. *Science* **377**, 292–297 (2022).
10. Forsberg, L. A. et al. Mosaic loss of chromosome Y in peripheral blood is associated with shorter survival and higher risk of cancer. *Nat. Genet.* **46**, 624–628 (2014).
11. Fadl-Elmula, I. et al. Karyotypic characterization of urinary bladder transitional cell carcinomas. *Genes Chromosomes Cancer* **29**, 256–265 (2000).
12. Sauter, G., Moch, H., Mihatsch, M. J. & Gasser, T. C. Molecular cytogenetics of bladder cancer progression. *Eur. Urol.* **33**, 9–10 (1998).
13. Smeets, W., Pauwels, R., Laarakkers, L., Debruyne, F. & Geraedts, J. Chromosomal analysis of bladder cancer. III. Nonrandom alterations. *Cancer Genet. Cytogenet.* **29**, 29–41 (1987).
14. Sauter, G. et al. DNA aberrations in urinary bladder cancer detected by flow cytometry and FISH. *Urol. Res.* **25**, S37–S43 (1997).
15. Neuhaus, M. et al. Polysomies but not Y chromosome losses have prognostic significance in pTa/pT1 urinary bladder cancer. *Hum. Pathol.* **30**, 81–86 (1999).
16. Siegel, R. L., Miller, K. D., Fuchs, H. E. & Jemal, A. Cancer statistics, 2021. *CA Cancer J. Clin.* **71**, 7–33 (2021).
17. Johansson, S. L. & Cohen, S. M. Epidemiology and etiology of bladder cancer. *Semin. Surg. Oncol.* **13**, 291–298 (1997).
18. Dumanski, J. P. et al. Smoking is associated with mosaic loss of chromosome Y. *Science* **347**, 81–83 (2015).
19. Tabayoyong, W. & Gao, J. The emerging role of immunotherapy in advanced urothelial cancers. *Curr. Opin. Oncol.* **30**, 172–180 (2018).
20. Rouanne, M. et al. Development of immunotherapy in bladder cancer: present and future on targeting PD(L)1 and CTLA-4 pathways. *World J. Urol.* **36**, 1727–1740 (2018).
21. Prokop, J. W. & Deschepper, C. F. Chromosome Y genetic variants: impact in animal models and on human disease. *Physiol. Genomics* **47**, 525–537 (2015).
22. Robertson, A. G. et al. Comprehensive molecular characterization of muscle-invasive bladder cancer. *Cell* **171**, 540–556.e525 (2017).
23. Lindskrog, S. V. et al. An integrated multi-omics analysis identifies prognostic molecular subtypes of non-muscle-invasive bladder cancer. *Nat. Commun.* **12**, 2301 (2021).
24. Gonzalez, J. R. et al. MADloy: robust detection of mosaic loss of chromosome Y from genotype-array-intensity data. *BMC Bioinformatics* **21**, 533 (2020).
25. Summerhayes, I. C. & Franks, L. M. Effects of donor age on neoplastic transformation of adult mouse bladder epithelium in vitro. *J. Natl Cancer Inst.* **62**, 1017–1023 (1979).
26. Chan, E., Patel, A., Heston, W. & Larchian, W. Mouse orthotopic models for bladder cancer research. *BJU Int.* **104**, 1286–1291 (2009).
27. White-Gilbertson, S., Davis, M., Voelkel-Johnson, C. & Kasman, L. M. Sex differences in the MB49 syngeneic, murine model of bladder cancer. *Bladder* **3**, e22 (2016).
28. Tu, M. M. et al. Targeting DDR2 enhances tumor response to anti-PD-1 immunotherapy. *Sci. Adv.* **5**, eaav2437 (2019).
29. Sugiura, K. & Stock, C. C. The effect of 2,4,6-triethylenimino-s-triazine on the growth of a variety of mouse and rat tumors. *Cancer* **5**, 979–991 (1952).
30. Gouin, K. H. 3rd et al. An N-cadherin 2 expressing epithelial cell subpopulation predicts response to surgery, chemotherapy and immunotherapy in bladder cancer. *Nat. Commun.* **12**, 4906 (2021).
31. Becht, E. et al. Dimensionality reduction for visualizing single-cell data using UMAP. *Nat. Biotechnol.* **37**, 38–44 (2019).
32. Hashimoto, M. et al. CD8 T cell exhaustion in chronic infection and cancer: opportunities for interventions. *Annu. Rev. Med.* **69**, 301–318 (2018).
33. Kwon, H. et al. Androgen conspires with the $CD8^+$ T cell exhaustion program and contributes to sex bias in cancer. *Sci. Immunol.* **7**, eabq2630 (2022).
34. Mariathasan, S. et al. TGFβ attenuates tumour response to PD-L1 blockade by contributing to exclusion of T cells. *Nature* **554**, 544–548 (2018).
35. Zhang, Q. et al. Mosaic loss of chromosome Y promotes leukemogenesis and clonal hematopoiesis. *JCI Insight* **7**, e153768 (2022).
36. Minner, S. et al. Y chromosome loss is a frequent early event in urothelial bladder cancer. *Pathology* **42**, 356–359 (2010).
37. Fabris, V. T. et al. Cytogenetic characterization of the murine bladder cancer model MB49 and the derived invasive line MB49-I. *Cancer Genet.* **205**, 168–176 (2012).
38. Ler, L. D. et al. Loss of tumor suppressor KDM6A amplifies PRC2-regulated transcriptional repression in bladder cancer and can be targeted through inhibition of EZH2. *Sci. Transl. Med.* **9**, eaai8312 (2017).
39. Walport, L. J. et al. Human UTY(KDM6C) is a male-specific *N*-methyl lysyl demethylase. *J. Biol. Chem.* **289**, 18302–18313 (2014).
40. Li, N. et al. JARID1D is a suppressor and prognostic marker of prostate cancer invasion and metastasis. *Cancer Res.* **76**, 831–843 (2016).
41. Seo, H. et al. TOX and TOX2 transcription factors cooperate with NR4A transcription factors to impose $CD8^+$ T cell exhaustion. *Proc. Natl Acad. Sci. USA* **116**, 12410–12415 (2019).
42. Khan, O. et al. TOX transcriptionally and epigenetically programs $CD8^+$ T cell exhaustion. *Nature* **571**, 211–218 (2019).
43. Thompson, D. J. et al. Genetic predisposition to mosaic Y chromosome loss in blood. *Nature* **575**, 652–657 (2019).

Methods

Cell culture

The parental MB49 cell line[44] was a gift from M. Burdick. Cell lines were authenticated by morphology and WES. All cell lines tested negative for mycoplasma contamination. The MB49 Y^- and Y^+ sublines were cultured in DMEM supplemented with 10% fetal bovine serum (FBS) and 0.1% sodium pyruvate. NA13 cell line was isolated from *N*-butyl-*N*-(4-hydroxybutyl) nitrosamine (BBN) carcinogen-induced bladder tumours of C57BL/6 female mice[45] and cultured in RPMI with 10% FBS. The E0771 breast cancer cell line E0771[28] (a gift from T. Lyons) was cultured in RPMI supplemented with 5% FBS. Single-cell isolations of MB49 Y^- and Y^+ cells were performed by serial dilution in 96-well plates.

In vivo tumour growth

Experiments were carried out at Cedar-Sinai Medical Center and The Ohio State University under protocols approved by the Institutional Animal Care and Use Committee (IACUC). Six- to eight-week-old male wild-type C57BL/6 and various syngeneic immunodeficient mice were purchased from Taconic or the Jackson Laboratory, and kept in a specific pathogen-free environment. Bladder cancer cell lines were detached, washed with PBS, and resuspended to make 10^6 cells per ml in phenol red-free DMEM media and left on ice. Animals were anaesthetized with isoflurane and cells were injected into the flank of each mouse subcutaneously (10^4 cells in 100 µl for MB49 sublines). The sample size in each experimental group was determined based on a previously published studies of similar models[45]. Mice were randomized to treatment groups and blinded to the researcher for the duration of the experiment. The same batch and number of cancer cells were injected per experiment, and all animals were housed under the same conditions. Investigators were blinded to group allocation during the experiment. Tumour length and width were measured using calipers, and tumour volume was calculated according to $(L \times W^2)/2$, where L is the largest diameter measurement of the tumour and W is the shortest perpendicular tumour measurement[45]. All analysis was performed consistently during all studies and all tumour counts were performed by the same investigator. For experiments involving PD-1 blockade, mice were treated with anti-PD-1 (200 µg, BioXCell clone 29F.1A12X) or isotype control IgG (200 µg) every 3 days starting when tumours reached ~100 mm^3.

Isolation of tumour-infiltrating T cells and high-dimensional flow cytometry

Endpoint Y^+ and Y^-, as well as CRISPR Y-Scr and CRISPR Y-KO MB49 tumours were mechanically disrupted and subjected to digestion via 1 mg ml^{-1} Collagenase D (Roche) for 30 min at 37 °C with agitation. Two percent bovine serum albumin in ice-cold PBS was used to inactivate enzymatic activity. Red blood cell lysis buffer (BioLegend) was used before cells were passed through 70 µm filters to generate single-cell suspensions. Cells were then stained at 4 °C with LIVE/DEAD blue fixable viability dye for 15 min (Invitrogen), followed by extracellular surface markers and FcR block concurrently for 40 min. All intracellular staining was performed using the FoxP3 transcription factor staining kit (Invitrogen) according to the manufacturer's instructions. All results were acquired on the Cytek Aurora, and fluorochrome-conjugated antibody panels were applied as previously described[33,46]. To analyse spectral flow cytometry results, live $CD45^+$ singlets were gated from samples stained with the 'all immune phenotyping' flow antibody panel (Fig. 3 and Supplementary Table 2) and live $CD45^+CD11b^-CD4^-CD8^+CD3^+$ singlets were gated from samples stained with the 'T cell exhaustion' panel (Fig. 5) using OMIQ to generate the presented UMAPs and heat maps.

In vitro cell proliferation and colony formation assays

Cell proliferation of MB49 sublines was determined using methyl thiazolyl diphenyl-tetrazolium bromide (MTT, Sigma). Different cell numbers (200–25,000) were seeded into 96-well plates with 150 µl of medium per well. Cells were assessed daily over an 8-day time course by adding MTT solution (1.25 mg ml^{-1} in DMEM) to cultures at a 1:1 ratio and incubating for two hours at 37 °C. Lysis buffer was added to dissolve the formazan crystals. Absorbance was read at 570 nm by a plate reader (BioTeK). MTT assays were performed three times in triplicate for each cell line tested. To check if Y chromosome specific genes were involved in anchorage-independent growth, soft agar colony formation assays were performed as previously described[47]. In brief, 15,000 cells per well in a 0.4 % agar (Sigma) were plated in triplicate in 6-well plates and cultured at 37 °C for 2 weeks. Colonies were stained with Nitro-BT (Sigma), and the images of the plates were captured under a microscope and analysed using ImageJ software.

Total RNA extraction and RT–qPCR

RNA was extracted from subcutaneous Y^+ and Y^- tumours or cell lysate using a RNeasy plus Mini Kit with gDNA Eliminator (Qiagen). Library preparation and RNA-seq was performed by Novogene (Sacramento, CA). cDNA was synthetized using Maxima H Minus cDNA Synthesis Master Mix (Thermo Scientific). Quantitative PCR was then performed using Quant Studio 6 Flex Real-Time PCR system (Applied Biosystems) via powerUp SYBR Green Master Mix (Applied Biosystems). Forward and reverse primer pairs used in RT–qPCR experiments are listed in the table below. To determine the changes in mRNA expression measured by RT–qPCR, the $\Delta\Delta C_t$ method was used. β-actin served as an internal control. The genes (forward primer/reverse primer) used are as follows: *Gapdh* (AACTTTGGCATTGTGGAAGG/ACACATTGGGGGTAGGAACA), *Actb* (TCATGAAGTGTGACGTTGACATCCGT/CCTAGAAGCATTTGCGGTGCACGATG), *Kdm5d* (CATGTAAAGGAGATAAGGAACT/ATGAATGCGCTCAGATTGGG), *Sry* (TCCTCAAAAGAAACCGTGCAT/AGATTAATGGTTGCTAAGGACTGGAT), *Ssty1* (CTGGAGCTCTACAGTGATGA/CAGTTACCAATCAACACATCAC), *Eif2s3y* (ATCTTGTCCTCAACCTCAGACT/TTCTTTAGCCTGGCTTTCTTTCA), *Uty* (TGGCCCTGATCGACTGTAAT/TGGTGCATCCAACCTAACTG), *Ddx3y* (TGTTAGTTGCCACACCAGGACG/TGGTGGCATTGTGTCCTGCTCA) and *Rbmy* (TGCTGGCTATCTTGGAGGACGT/GCGGTTGTTTCCACCTCTTGCA).

RNA-seq data analysis

Illumina Truseq adapter, polyA, and polyT sequences were trimmed with cutadapt v2.3[48]. Trimmed reads were aligned to mouse genome version 38 (mm10) using STAR aligner v2.7.0d_0221[49] with parameters according to the ENCODE long RNA-seq pipeline (https://github.com/ENCODE-DCC/long-rna-seq-pipeline). Gene expression levels were quantified using RSEM v1.3.1[50]. Ensembl gene annotations (version 84) were used in the alignment and quantification steps. RNA-seq sequence, alignment and quantification quality was assessed using FastQC v0.11.5 and MultiQC v1.8 (ref. 51). Biological replicate concordance was assessed using PCA and pairwise Pearson correlation analysis. Low expressed genes were filtered out by applying the following criterion: estimated counts (from RSEM) ≥ number of samples × 5. Filtered estimated read counts from RSEM were compared using the R Bioconductor package DESeq2 v1.22.2 based on generalized linear model and negative binomial distribution[52]. Genes with Benjamini–Hochberg corrected P value < 0.05 and fold change ≥ 1.5 or ≤ −1.5 were selected as DEGs.

Engineering of UTY and KDM5D expression in MB49 cells

CRISPR–Cas9 editing of *UTY* and *KDM5D* in Y^+ MB49 cells. CRISPR–Cas9 KO plasmids were purchased from Santa Cruz. *UTY* CRISPR–Cas9 KO plasmid (m2) was a pool of 3 different guide RNA (gRNA) plasmids: A, sense: TCTTTAATAGTAAAAGCTGA (sc-423636-KO-2); B, sense: GATGAAGACGCTGTTGAACA (sc-423636-KO-2); and C, sense: ACAGTTTACAGACTGACTAC (sc-423636-KO-2). *KDM5D* (SmcY) CRISPR–Cas9 KO plasmid (m) was a pool of three different gRNA plasmids: A, sense:

GGACCTTTACAGCCTTAATA (sc-423031); B, sense: TTCAGTTGCTAC AGTAGACG (sc-423031); and C, sense: TCATTTAGCCTCTGAATTCG (sc-423031). The control was a non-targeting gRNA (not targeting any known gene; sc-418922). CRISPR–Cas9 plasmids were transfected into Y^+ MB49 cells using UltraCrus transfection reagent according to the manufacturer's instruction (Santa Cruz). Forty-eight hours after transfection, the medium was aspirated and replaced with fresh medium containing puromycin for selection. For validation of knockout cells, single cells were isolated as described above. RNA from each clone (using a RNeasy kit) was used to validate knockout of *UTY* or *KDM5D*.

Overexpression of *UTY* and *KDM5D* in MB49 Y^- cells. Plasmid ps100001 from Origene was used to overexpress *KDM5D* and *UTY*. Empty vector served as the negative control. Lipofectamine 3000 (Thermo Fisher) was used for all transfections according to the manufacturer's protocol. Forty-eight hours after transfection, the medium was replaced with fresh medium containing neomycin for selection.

Genomic DNA isolation and whole-exome sequencing. Genomic DNA was isolated from parental, Y^- and Y^+ MB49 cell lines using a kit from Invitrogen (catalogue no. K1820) according to the manufacturer's instructions. DNA samples were submitted for sequencing at Novogene. Library preparation, sequencing and bioinformatics analysis were performed by Novogene. In brief, all samples were sent for WES and the sequencing data processed using the GATK best practice workflow[53]. The genomic DNA was randomly sheared into short fragments, end-repaired, A-tailed, and ligated with Illumina adapters. After PCR amplification, size selection, and purification, we proceeded with the hybridization capture of libraries. The captured libraries were enriched by PCR amplification and checked with Qubit and bioanalyzer for quality control. The libraries were then pooled and sequenced on Illumina platforms using the PE150 strategy. We mapped the paired-end clean reads to the mouse reference genome (Mouse, NCBI37/mm9) using BWA, sorted them with Sambamba, and marked duplicates with Picard. Finally, we computed the coverage and depth, and tested for SNP and InDel detection.

Generation of the CRISPR–Cas9-mediated Y chromosome KO MB49. Plasmids: gRNA targeting the centromere of the Y chromosome (LOY_gRNA1_fwd CACCGGAGTTAATATAAAAAACA and LOY_gRNA1_rv AAACTGTTTTTTATATTAACTCC) alongside the non-targeting control gRNA (Control_(Neo)_gRNA1_fwd CACCGGCAGCGCGGCTATCGTGGC and Control_(Neo)_gRNA1_rv AAACGCCACGATAGCCGCGCTGCC) were a gift from K. Walsh[9]. LentiCRISPRv2 neo, Cas9 plasmid #98292; pLKO5.0.sgRNA.EFS.tRFP, plasmid #57823; psPAX2; plasmid #12260; and pMD2.G, plasmid #12259 were purchased from Addgene.

For lentivirus production, HEK 293T cells were seeded at a density of 4×10^6 cells per 10 cm^2 plate in DMEM + 5% FBS and incubated at 37 °C, 5% CO_2. The plasmids (5 μg of lentiCRISPRv2 neo or pLKO5.0.sgRNAs. EFS.tRFP, 4.17 μg psPAX2, and 0.83 μg of pMD2.G per plate) were co-transfected using HEK 293T cells with Trans-IT transfection reagent (Mirus). Culture supernatant was collected 48 h after transfection, centrifuged, and filtered through a 0.45-μm filter. To Generate Cas9-stable Y^+ MB49 cells, Y^+ MB49 cells were transduced with lentivirus containing Cas9 plasmid (lentiCRISPRv2 neo) and selected with Geneticin (G418). Given that the LOY gRNA plasmid also contains a turbo red fluorescent protein (tRFP) marker, we sorted the cells based on tRFP 48 h after transduction into 96 wells using BD Symphony S6 cell sorter for further culturing. Single-cell clones were expanded and screened for knockout of the Y chromosome by RT–qPCR. Control cells were generated by transducing Cas9 Y^+ MB49 cells with control gRNA.

Nanostring GeoMx digital spatial profiling

Haematoxylin and eosin (H&E) images of Y^+ and Y^- MB49 tumours were demarcated by a clinical pathologist (Cedars-Sinai Biobank Core) for regions in each core to generate a tumour microarray (TMA). Five-micrometre sections were cut from the TMA block, stained and analysed on the Nanostring GeoMx digital spatial profiling platform at the Cedars-Sinai Biobank Core per the manufacturer's instructions[54]. The protein panel consisted of 68 antibodies, including mouse immune cell profiling, immuno-oncology drug targets, immune activation, immune cell typing, pan-tumour and cell death markers (Extended Data Fig. 6a). S6 ribosomal protein and histone 3 were included in the panel as housekeeping proteins.

One region of interest (ROI) per core was selected by aligning fluorescent images with H&E images predetermined by a pathologist. Regions with blood vessels and necrosis were kept to a minimum. ROI selection on each TMA core was performed such that 660-μm circles were segmented into cytokeratin$^+$ (tumour) and cytokeratin$^-$ (stroma) regions. Barcodes from these regions were collected to generate measurements per compartment. Barcodes were sequenced, mapped, and counted by next-generation sequencing (NGS) readouts as per manufacturer's instructions. Antibody barcodes were counted on an Ncounter platform per manufacturer's instructions, enabling quantitative comparisons of antibodies between ROIs in Y^+ and Y^- subcutaneous tumours.

The GeoMx digital spatial profiling analysis suite (GEOMX-0069) allowed inspection, quality control (QC), normalization, and differential expression to be performed. In brief, normalization using Histone H3 and S6 proteins was performed. Differential expression between paired compartments was evaluated by paired *t*-tests with a Benjamini–Hochberg correction, while differential expression between unpaired compartments was performed by a Mann–Whitney test with Benjamini–Hochberg correction. GraphPad prism software version 8.0 (GraphPad Prism) was used for all of the statistical analyses. The student's two tailed *t*-test was used to analyse all comparisons, with a Bonferroni adjustment for multiple comparisons when appropriate.

Y signature score

A gene expression signature score was created based on 18 Y-encoded genes expressed in normal bladder urothelium as previously reported (Extended Data Fig. 1b)[2,21]. The Y signature was obtained by the single sample gene set enrichment analysis[55] (ssGSEA, package GSEApy v0.10.1) according to 18 important Y chromosome genes expressed in each of the bulk RNA-seq samples from TCGA data, IMvigor210 cohorts, and the E-MTAB-4321 cohort. For the snRNA-seq dataset, we used Scanpy (scanpy.tl.score_genes function; scanpy v1.9.1)[56] to get the Y signature for each patient. The score is the average expression of a set of genes subtracted by the average expression of a reference set of genes which is randomly sampled from the gene pool for each binned expression value. Y chromosome signature scores were compared to two virtual karyotyping techniques, EDY using TCGA RNA data[1] and MADLOY using TCGA DNA sequencing data[24].

Gene set enrichment analysis

Genes that were differentially expressed in specific sample groups were identified using DESeq2 software (version 1.26.0)[52] with the Wald test by using a design formula that included batch effect correction. Benjamini–Hochberg correction was used for multiple testing in all instances. We performed gene set enrichment analysis (GSEApy v0.10.1)[55] to identify significantly differentially enriched pathways between the Y^+ and Y^- MB49 cell lines and tumours. The gene ontology gene set in the MSigDB database was used as the reference gene set. The default weighted enrichment statistical method was applied to the enrichment analysis, and the number of the gene set permutations for each analysis was set at 1,000. Statistical significance was set at a |normalized enrichment score| > 1, nominal P value < 0.05.

Human bladder cancer RNA-seq datasets

We performed differential gene expression analyses on publicly available urothelial bladder cancer datasets from the IMvigor210 clinical trial[57], TCGA and NMIBC E-MTAB-4321 datasets[58]. For the analysis involving IMvigor210, only male pre-chemotherapy bladder cancer samples

were used. Objective response rate, important signature score and survival data for each male patient was extracted using the R package IMvigor210CoreBiologies. For the TCGA analysis, the data levels, and the files contained in each data level package, are described below and are present on the NCI Genomic Data Commons. We estimated cell population abundance in the TCGA MIBC samples using the MCP counter method, which uses transcriptomic data to deconvolute and quantify the abundance of various immune cell types[59]. For the snRNA-seq analyses, data for 21 treatment-naive male patients with MIBC from our previous study[30], with surgery (transurethral resection of bladder tumour or cystectomy) as their only treatment, can be downloaded from the Gene Expression Omnibus (GSE169379 and GSE171351) in our previous study. To explore this transcriptional heterogeneity, we classified single cells using the ProjecTILs[60] T cell atlas derived from tumour-infiltrating T cells. The atlas consists of 16,803 high-quality single-cell transcriptomes from 25 samples (B16 melanoma and MC38 colon adenocarcinoma tumours) from six different studies[61–67].

CODEX

We obtained our patient-matched CODEX data from our same bladder cancer snRNA-seq study[30], Processed CODEX data can be downloaded from https://figshare.com/s/4610a15363c8306dfa36, https://figshare.com/s/2005255a8b65de23109f and https://figshare.com/s/1d8c7ed76d4b3222ada4.

The CODEX technology enables highly multiplexed analysis for up to 40 proteins using cyclic detection of DNA-indexed antibody panels. In this study, CODEX was grouped according to Y signature, which was obtained based on the snRNA-seq data of 21 male patients with bladder cancer. Seven patients with high scores were selected as the Y_{high} group (>0.2 mean Y signature score) and 7 patients with low scores were selected as the Y_{low} group (<0.2 mean Y signature score). CODEX-stained cells were manually gated based on the intensity of PanCytoK, CD45, aSMA, CD31, CD20, CDH12, CDH18, CD68, CD3e, CD8 and CD4 into a training set consisting of broad cell types: epithelial, epithelial KRT, epithelial CDH, stromal, endothelial, general $CD45^+$ immune, B cell, $CD8^+$ T, $CD4^+$ T and macrophage.

Kaplan–Meier analyses

Clinical outcomes were assessed using Kaplan–Meier survival curves and log-rank or Cox statistics. Kaplan–Meier survival analysis was performed using the survminer package in R software. The function surv_cutpoint in the R package survminer was implemented to discover the optimal cut-off value for the Y chromosome signature. This R package determines the optimal cut-off point for one or multiple continuous variables at once, using the maximally selected rank statistics from the maxstat R package. This is an outcome-oriented method providing a value of a cut-point that corresponds to the most significant relation with survival.

Quantification of tumour neoantigen burden

For each patient in the IMvigor210 and TCGA databases, we first enumerated a list of all possible 9 and 10-mer peptides bearing somatic mutations or overlapping open reading frames derived from frameshifting indels or nonstop mutations. These peptides were then evaluated for binding against the patient's inferred HLA type using the NetMHCpan-3.0 algorithm[68]. The neoantigen load was defined as the total number of predicted peptide:allele binders with a rank percentile score less than or equal to the weak binder threshold (2%).

Statistical analyses

The statistical tests employed, the number of replicates, and independent experiments are specified in the text and figure legends. Basic statistical analysis was performed using GraphPad/Prism (v.9.0), while R (versions 4.1.2 or 4.2.3) and Python 3.9.4 were used for analyses of epidemiological and mutation and sequence data. Prior to conducting any statistical test, a Kolmogorov–Smirnov normality test was performed, and Bartlett or Levene tests were used to evaluate the assumption of homogeneity of variances. The unpaired Student's *t*-test was applied to normally distributed variables, while the Mann–Whitney *U* test (also known as the Wilcoxon rank-sum test) was employed for non-normally distributed variables. Pearson's Chi-squared test was used for analysing categorical data, with the R function chisq.test used for chi-squared analyses and wilcox.test used for Wilcoxon rank-sum tests. Significance levels were denoted using asterisks, with NS indicating non-significance. In cases where multiple hypotheses were tested, FDR correction was applied. Data analysis software such as Scanpy (v.1.7.2), Pandas (v.2.0.0), Conda (v.4.11.0), NumPy (v.1.24.2) and Scipy (v.1.10.1) was used. The R package ComplexHeatmap (v.2.11.1) was used to generate heat maps, while ggplot2 (v.3.3.5), ggpubr (v.0.6.0), and ggrepel (v.0.9.2) R packages were used for general visualization purposes.

Reporting summary

Further information on research design is available in the Nature Portfolio Reporting Summary linked to this article.

Data availability

The data supporting the findings of this study are available within the article, extended data and supplementary information files. RNA-seq and WES data are available at the Gene Expression Omnibus with accession reference GSE229233 and GSE230820. Source data are provided with this paper.

44. Lattime, E. C., Gomella, L. G. & McCue, P. A. Murine bladder carcinoma cells present antigen to BCG-specific $CD4^+$ T-cells. *Cancer Res.* **52**, 4286–4290 (1992).
45. Tu, M. M. et al. Inhibition of the CCL2 receptor, CCR2, enhances tumor response to immune checkpoint therapy. *Commun. Biol.* **3**, 720 (2020).
46. Song, N. J. et al. Treatment with soluble CD24 attenuates COVID-19-associated systemic immunopathology. *J. Hematol. Oncol.* **15**, 5 (2022).
47. Richmond, C. S. et al. Glycogen debranching enzyme (AGL) is a novel regulator of non-small cell lung cancer growth. *Oncotarget* **9**, 16718–16730 (2018).
48. Martin, M. Cutadapt removes adapter sequences from high-throughput sequencing reads. *EMBnet J.* **17**, 10–12 (2011).
49. Dobin, A. et al. STAR: ultrafast universal RNA-seq aligner. *Bioinformatics* **29**, 15–21 (2013).
50. Li, B. & Dewey, C. N. RSEM: accurate transcript quantification from RNA-Seq data with or without a reference genome. *BMC Bioinformatics* **12**, 323 (2011).
51. Ewels, P., Magnusson, M., Lundin, S. & Kaller, M. MultiQC: summarize analysis results for multiple tools and samples in a single report. *Bioinformatics* **32**, 3047–3048 (2016).
52. Love, M. I., Huber, W. & Anders, S. Moderated estimation of fold change and dispersion for RNA-seq data with DESeq2. *Genome Biol.* **15**, 550 (2014).
53. DePristo, M. A. et al. A framework for variation discovery and genotyping using next-generation DNA sequencing data. *Nat. Genet.* **43**, 491–498 (2011).
54. Hernandez, S. et al. Challenges and opportunities for immunoprofiling using a spatial high-plex technology: the NanoString GeoMx((R)) digital spatial profiler. *Front. Oncol.* **12**, 890410 (2022).
55. Hänzelmann, S., Castelo, R. & Guinney, J. GSVA: gene set variation analysis for microarray and RNA-seq data. *BMC Bioinformatics* **14**, 7 (2013).
56. Wolf, F. A., Angerer, P. & Theis, F. J. SCANPY: large-scale single-cell gene expression data analysis. *Genome Biol.* **19**, 15 (2018).
57. Rosenberg, J. E. et al. Atezolizumab in patients with locally advanced and metastatic urothelial carcinoma who have progressed following treatment with platinum-based chemotherapy: a single-arm, multicentre, phase 2 trial. *Lancet* **387**, 1909–1920 (2016).
58. Hedegaard, J. et al. Comprehensive transcriptional analysis of early-stage urothelial carcinoma. *Cancer Cell* **30**, 27–42 (2016).
59. Becht, E. et al. Estimating the population abundance of tissue-infiltrating immune and stromal cell populations using gene expression. *Genome Biol.* **17**, 218 (2016).
60. Andreatta, M. et al. Interpretation of T cell states from single-cell transcriptomics data using reference atlases. *Nat. Commun.* **12**, 2965 (2021).
61. Bassez, A. et al. A single-cell map of intratumoral changes during anti-PD1 treatment of patients with breast cancer. *Nat. Med.* **27**, 820–832 (2021).
62. Daud, A. I. et al. Tumor immune profiling predicts response to anti-PD-1 therapy in human melanoma. *J. Clin. Invest.* **126**, 3447–3452 (2016).
63. Gros, A. et al. PD-1 identifies the patient-specific $CD8^+$ tumor-reactive repertoire infiltrating human tumors. *J. Clin. Invest.* **124**, 2246–2259 (2014).
64. Miller, B. C. et al. Subsets of exhausted $CD8^+$ T cells differentially mediate tumor control and respond to checkpoint blockade. *Nat. Immunol.* **20**, 326–336 (2019).
65. Siddiqui, I. et al. Intratumoral $Tcf1^+PD\text{-}1^+CD8^+$ T cells with stem-like properties promote tumor control in response to vaccination and checkpoint blockade immunotherapy. *Immunity* **50**, 195–211.e110 (2019).
66. Thommen, D. S. et al. A transcriptionally and functionally distinct $PD\text{-}1^+CD8^+$ T cell pool with predictive potential in non-small-cell lung cancer treated with PD-1 blockade. *Nat. Med.* **24**, 994–1004 (2018).

67. Kumagai, S. et al. The PD-1 expression balance between effector and regulatory T cells predicts the clinical efficacy of PD-1 blockade therapies. *Nat. Immunol.* **21**, 1346–1358 (2020).
68. Nielsen, M. & Andreatta, M. NetMHCpan-3.0; improved prediction of binding to MHC class I molecules integrating information from multiple receptor and peptide length datasets. *Genome Med.* **8**, 33 (2016).

Acknowledgements This work was supported in part by NIH P01CA278732 and R01CA143971 to D.T. and NIH R01CA262069, R01CA262388 and R01AI077283 to Z.L. J.M.S. and T.D.G. were supported by the Ohio State University Comprehensive Cancer Center's Tumor Immunology T32 (2T32CA09223-16A1) post-doctoral fellowship award. We thank K. Walsh for providing the LOY gRNA plasmids, and N.-J. Song and B. Riesenberg for development of the 'all immune phenotyping' flow antibody panel. We acknowledge resources from the Immune Monitoring and Discovery Platform and the Pelotonia Institute for Immuno-Oncology at OSU Comprehensive Cancer Center (P30CA016058).

Author contributions The study was initiated by H.A.A.-H. and D.T. H.A.A.-H., J.M.S., X.C., T.X. and T.D.G. developed methodology. H.A.A.-H., J.M.S., X.C., T.X. and T.D.G. acquired data. H.A.A.-H. generated the MB49 cell line models and conducted the wild-type versus immune-compromised mouse model experiments. J.M.S. conducted the Y^+ versus Y^- mouse experiments and associated flow cytometry studies. T.X. and T.D.G. conducted the CRISPR Y-Scr and CRISPR Y-KO mouse experiments and associated flow cytometry studies. X.C. performed the human sample biostatistical analyses and associated graph generations. H.A.A.-H., J.M.S., X.C., T.X., T.D.G., Z.L. and D.T. analysed and interpreted data. H.A.A.-H., J.M.S., Z.L. and D.T. wrote the manuscript. D.T. and Z.L. supervised the study. All authors reviewed and approved the final manuscript.

Competing interests Z.L. reports personal consultation fees from Alphamab, HanchorBio, Henlius, Heat Biologic and Ikonisys outside the submitted work. All other authors declare no competing interests.

Additional information

Supplementary information The online version contains supplementary material available at https://doi.org/10.1038/s41586-023-06234-x.

Correspondence and requests for materials should be addressed to Dan Theodorescu.

Peer review information *Nature* thanks Mitchell Machiela, Soichi Sano and the other, anonymous, reviewer(s) for their contribution to the peer review of this work.

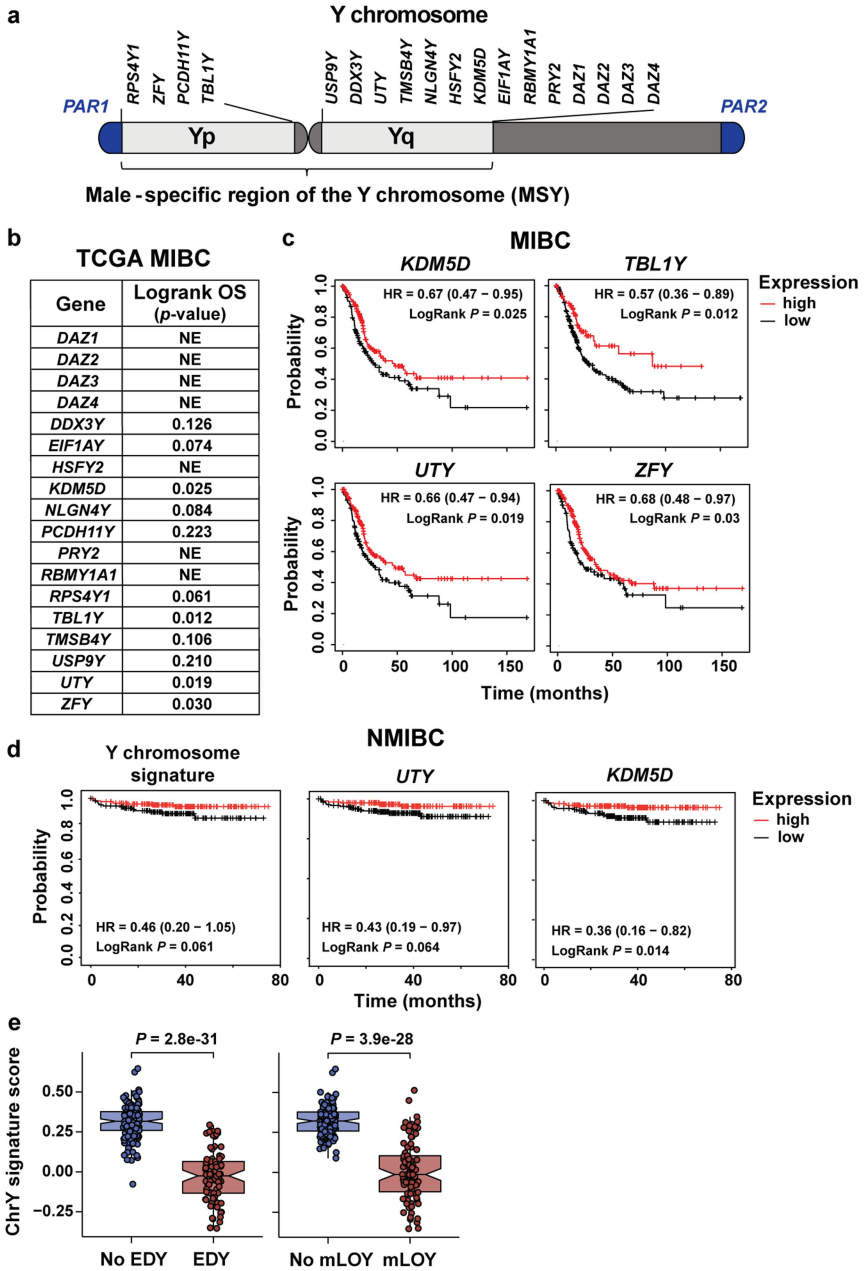

Gene	Logrank OS (*p*-value)
DAZ1	NE
DAZ2	NE
DAZ3	NE
DAZ4	NE
DDX3Y	0.126
EIF1AY	0.074
HSFY2	NE
KDM5D	0.025
NLGN4Y	0.084
PCDH11Y	0.223
PRY2	NE
RBMY1A1	NE
RPS4Y1	0.061
TBL1Y	0.012
TMSB4Y	0.106
USP9Y	0.210
UTY	0.019
ZFY	0.030

Extended Data Fig. 1 | LOY is associated with a worse clinical outcome for patients with MIBC and NMIBC. a, Y chromosome genes expressed in normal bladder urothelium that were used to create a Y chromosome gene expression signature. **b**, Logrank *p*-values based on stratification by Y chromosome gene expression (normalized FPKM) on TCGA MIBC patient overall survival (OS). Genes resulting in statistically significant OS are plotted in panel **c**. NE, not expressed. **c**, Kaplan-Meier plots of OS from TCGA data for males with MIBC and either high or low *KDM5D*, *TBL1Y*, *UTY* (*KDM6C*), or *ZFY* expression. **d**, Kaplan-Meier survival curves stratified by the Y signature score or expression levels for *UTY* and *KDM5D* in NMIBC from the E-MTAB-4321 cohort. Survival differences are based on Logrank statistics. **e**, ChrY gene expression signature scores of TCGA data plotted with respect to extreme downregulation of chromosome Y (EDY, left panel) and Mosaic Alteration Detection for LOY (mLOY, right panel) levels. Statistical significance was determined by Wilcoxon rank-sum test (NoLOY n = 151, LOY n = 90, NoEDY n = 165, EDY n = 76). Boxplots represent the mean with first and third quartile data. Minimum and maximum datapoints are included.

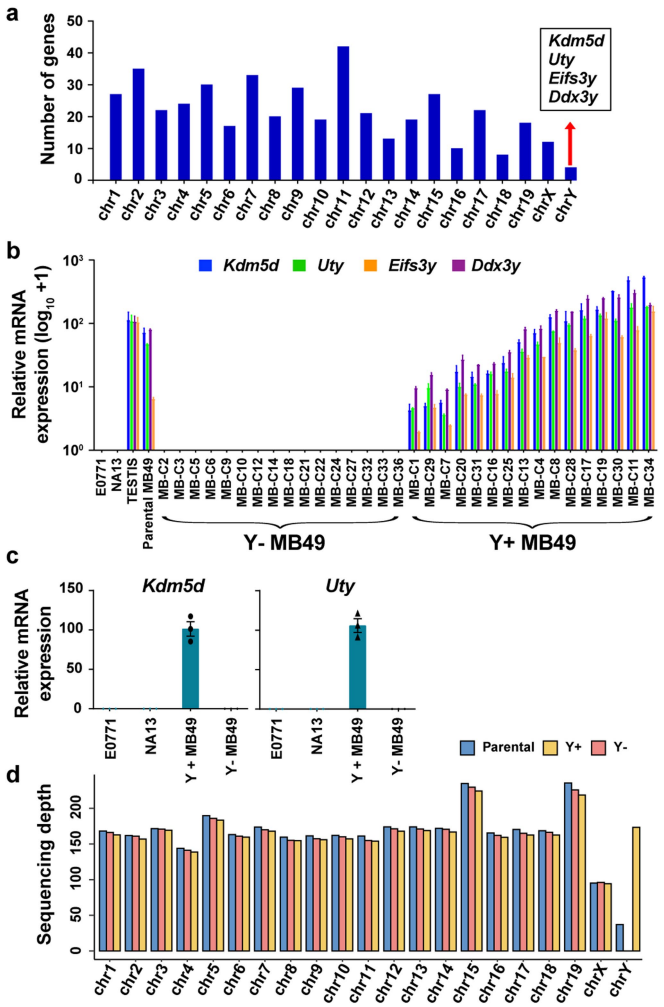

Extended Data Fig. 2 | Generation of Y+ and Y- BC models. a, Histogram representation of deferentially regulated genes (DEG) from Y+ vs. Y- MB49 RNAseq data per mouse chromosome. **b**, qRT-PCR analysis of *Uty*, *Kdm5d*, *Eifs3y*, and *Ddx3y* expression in MB49 clones isolated from the parental MB49 compared to female murine breast cancer (E0771) and bladder cancer cells (NA13), and testis tissue. Curly brackets indicate the clonal lines used to generate the pooled Y+ and Y- MB49 sublines. **c**, qRT-PCR analysis of *Uty and Kdm5d* expression in the pooled Y+ and Y- sublines described in **a**. n = 3 biological replicates. Data are mean ± s.e.m. **d**, Bar graph of sequencing depth for each chromosome after performing whole exome sequencing (WES) on DNA from the Parental, Y-, and Y+ MB49 cell lines.

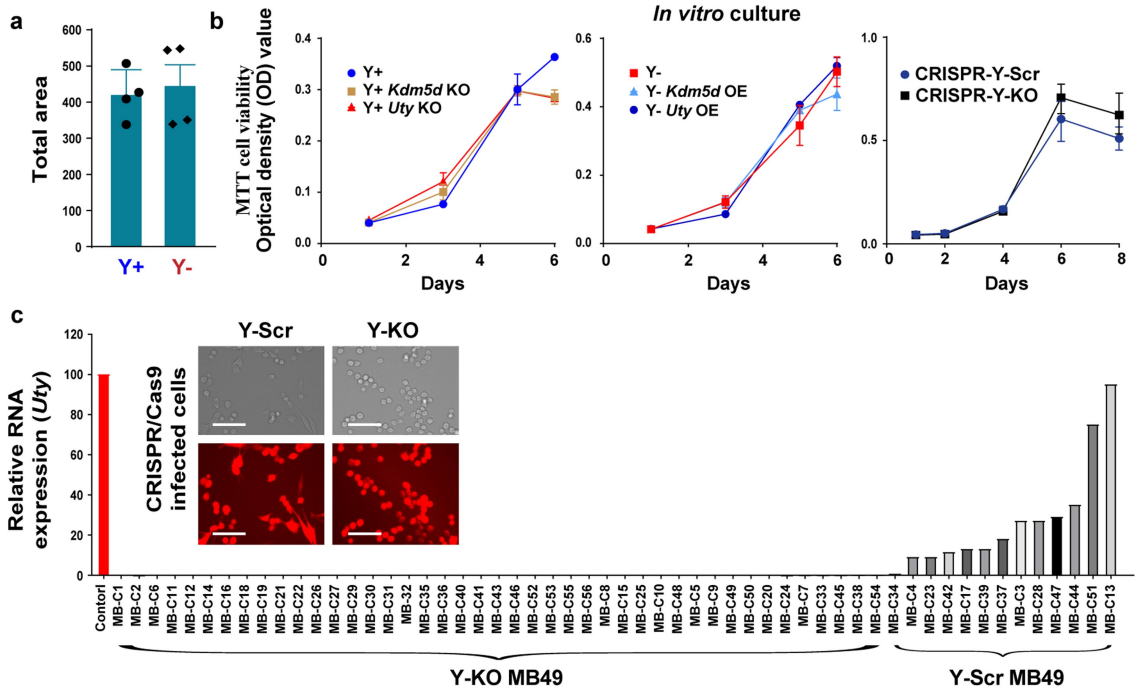

Extended Data Fig. 3 | LOY has no effect on colony forming ability of BC in vitro. a, MB49 Y+ and Y- cells were grown in 0.4% agar for two weeks. Colonies were stained with Nitro-BT and quantified using ImageJ. Average colony number and area were determined from those with a diameter that exceeded 100 µm (n = 4 biological replicates). Data representative of three independent experiments. Statistical significance was determined by two-sided unpaired *t*-test, *P*-value = 0.722. Data are mean ± s.e.m. **b**, In vitro cell proliferation (MTT cell viability) over a 6–8-day time course using three sets of genetically engineered MB49 cells: Y+, Y+ *Kdm5d* KO, Y+ *Uty* KO (left panel), Y-, Y- *Kdm5d* OE, Y- *Uty* OE (middle panel), and CRISPR-Y-Scr vs. CRISPR-Y-KO (right panel). n = 3 biological replicates. Data are mean ± s.e.m. **c**, qRT-PCR analysis of *Uty* expression in MB49 clones isolated from the CRISPR-generated Y-KO and Y-Scr MB49 cell lines. Curly brackets indicate the clonal lines used to generate the pooled Y+ Control and Y- KO MB49 sublines. Representative immunofluorescence images of the CRISPR-generated Y-KO and Y-Scr MB49 cell lines. Scale bar, 150 µM.

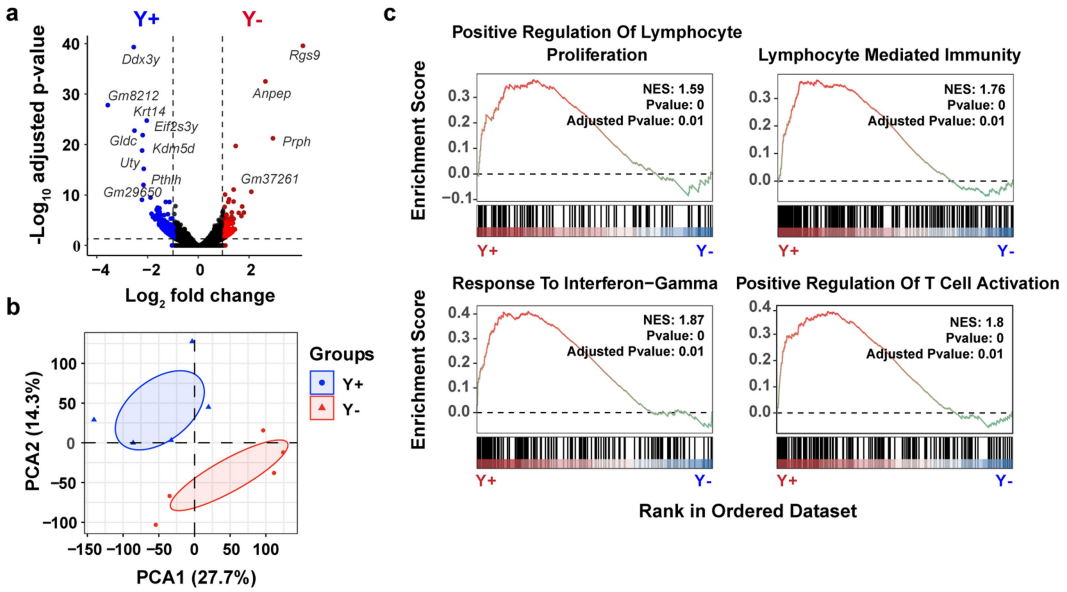

Extended Data Fig. 4 | Increased lymphocyte activation in Y+ tumors. **a**, Volcano plot of DEGs from bulk RNA isolated from Y+ and Y- MB49 tumors grown in male WT mice. Blue (Y+ tumors) and red (Y- tumors) genes correspond to statistically significant (Benjamini-Hochberg method, $P < 0.05$) genes that have a $|>1 \log_2|$ fold-change in expression. **b**, PCA of DEGs described in **a**. **c**, Gene ontology (GO) pathway enrichment score plots of statistically significant gene set enrichment analyses (GSEA) using DEGs from **a**. NES, normalized enrichment score.

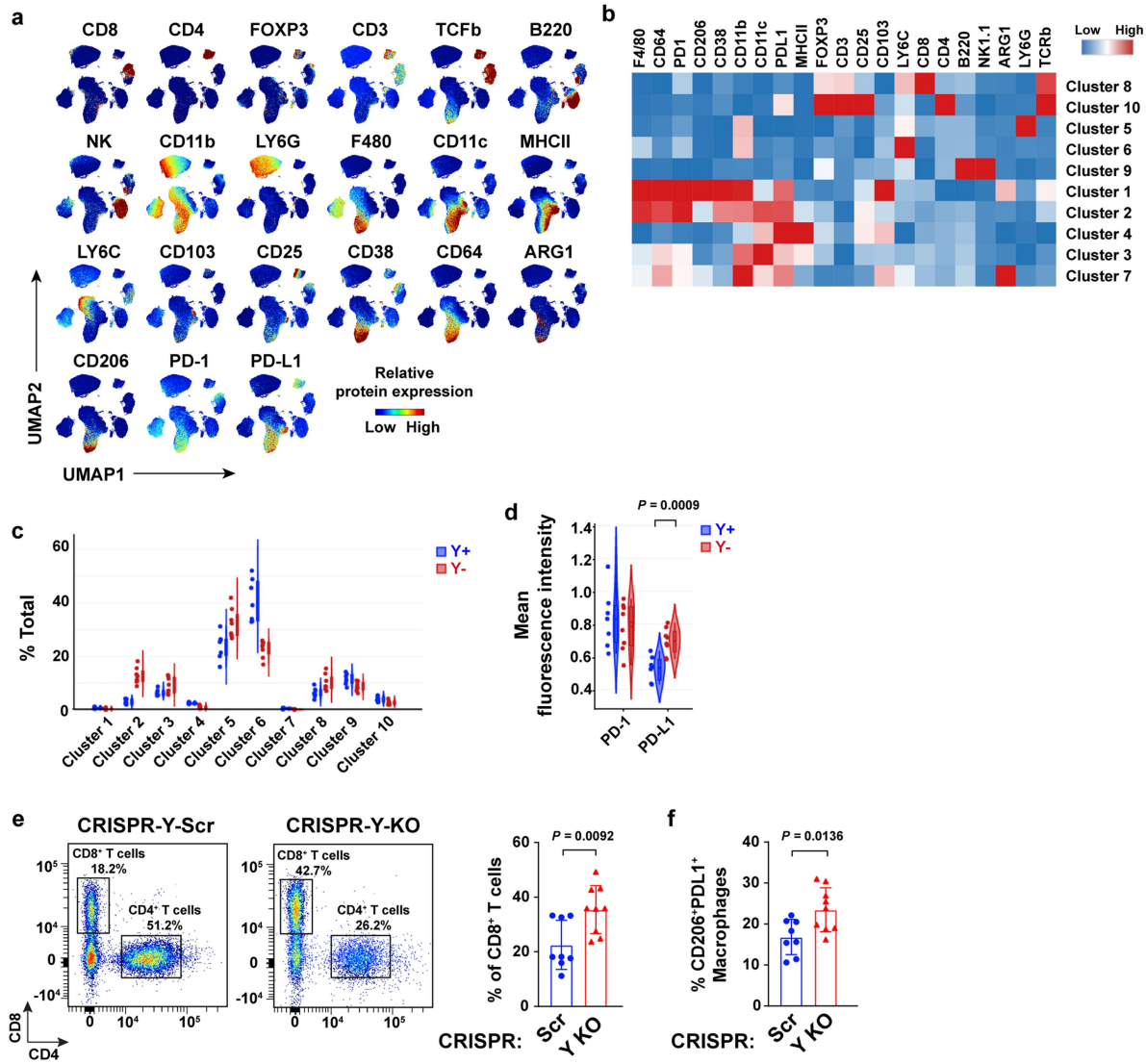

Extended Data Fig. 5 | Comprehensive immune phenotyping of tumor-infiltrating leukocytes (TILs) in Y+ and Y- MB49 tumors. a, UMAPs demonstrating individual spectral flow cytometry analysis of protein marker expression in CD45$^+$ immune cells isolated from Y+ and Y- MB49 tumors grown in WT male mice. **b**, Heatmap of relative protein expression from immune cells described in **a**. **c**, Violin plots of each tumor sample across each cluster from the CD45$^+$ immune cell UMAP (see Fig. 3b). **d**, Violin plot of PD-1 and PD-L1 mean fluorescence intensity in CD45$^+$ immune cells from Y+ and Y- MB49 tumors. **e**, Representative dot plots and percentages of CD8$^+$ and CD4$^+$ T cells gated on total CD3$^+$ T cells from CRISPR-Y-Scr (n = 8) and CRISPR-Y-KO (n = 9), MB49 tumors grown for 22 or 17 days, respectively, in male WT mice (left panels). Percentage of CD8$^+$ T cells of total CD3$^+$ T cells per tumor sample (right panel). **f**, Percentage of CD206$^+$PDL1$^+$ macrophages among total CD11b$^+$F4/80$^+$ macrophages from Control and Y KO MB49 tumors described in **e**. Statistics were determined using two-sided unpaired *t*-tests.

a

Controls	Immune Cell Profiling	iO Drug Target	Immune Activation Status	Immune Cell Typing	Pan-Tumor Module	Cell Death Module
Rb IgG	PD-1	LAG3	CD127/IL7RA	CD14	IFNGR	BAD
Rt IgG2a	MHC II	OX40L	CD27	CD163	EPCAM	Cleaved Casp 3
Rt IgG2b	CD11b	TIM3	CD40	CD31	S100B	BCLXL
Histone H3	KI-67	VISTA	CD40L	CD34	ER	Gamma-H2AX
S6	F4/80	B7-H3	ICOS	FOXP3	AhR	p21
GAPDH	CD11c	GITR	CD44	Ly6G/Ly6C	AR	NF1
	CD19		CD86	BATF3	GFP	p53
	CD3e			CD28	PMEL17	PERFORIN
	CD4				HER2	PARP
	CD45					BIM
	CD8a					
	CTLA4					
	GZMB					
	PD-L1					
	PanCk					
	SMA					
	Fibronectin					

b

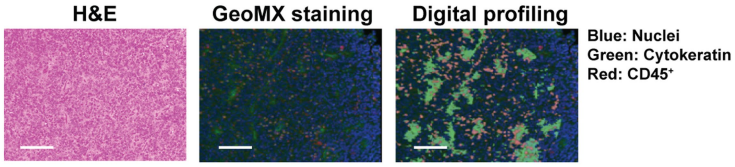

c

Target name	Log2	*P*-value
CD45	0.510	**0.009**
Tim-3	0.603	**0.016**
AhR	0.580	**0.018**
F4/80	-0.543	**0.026**
MHC II	0.810	**0.030**
CD31	0.482	0.056
BCLXL	0.345	0.060
VISTA	0.773	0.075
PD-L1	-0.434	0.089
Ki-67	0.312	0.096
BatF3	0.338	0.098
GZMB	0.485	0.121
p21	0.458	0.125
CD40L	0.448	0.129
PD-1	-0.372	0.129
HER2	0.346	0.161
PanCk	0.423	0.174
LAG3	0.387	0.188
IFNGR	0.236	0.207
Cleaved Caspase 3	0.725	0.213
OX40L	0.397	0.217
CD40	0.338	0.235
FOXP3	0.303	0.254
CD11b	0.777	0.264
BAD	0.170	0.285
CD86	0.325	0.309
CD11c	0.388	0.313
AR	0.284	0.331

Target name	Log2	*P*-value
CD44	0.401	0.335
Ly6G/Ly6C	0.626	0.335
CD14	-0.115	0.342
S100B	0.275	0.354
PARP	0.286	0.359
CD127/IL7RA	0.110	0.361
CD4	0.030	0.393
Perforin	0.555	0.394
BIM	0.132	0.441
gamma-H2AX	-0.230	0.541
GITR	0.259	0.545
Epcam	0.168	0.546
CD34	-0.035	0.555
CTLA4	0.105	0.564
SMA	0.218	0.640
CD27	0.143	0.646
Pmel17	0.001	0.657
p53	-0.077	0.677
CD8a	0.055	0.734
CD3e	-0.112	0.776
ER	-0.013	0.789
CD28	0.091	0.797
ICOS	0.139	0.814
CD19	0.165	0.819
CD163	0.435	0.827
Fibronectin	0.125	0.914
GFP	0.236	0.929
B7-H3	0.128	0.950

Extended Data Fig. 6 | GeoMX histological evaluation of infiltrating immune cells in Y- and Y+ MB49 tumors. a, Table of markers that are functionally categorized for GeoMX evaluation of Y+ and Y- MB49 tumors. **b**, Representative H&E image (left), immunofluorescence detection of nuclei (blue), cytokeratin (green), $CD45^+$ immune cells (red) (middle), and associated computational digital profiling (right) to quantify markers shown in **a**. Scale bar, 125 μM. **c**, Quantification (log_2 fold change and *P*-value) of the markers listed in Y+ versus Y- MB49 tumors (n = 10 tumors per group and three TMA cores per tumor). Data representative of two independent experiments. Statistical significance was determined by two-sided unpaired *t*-test.

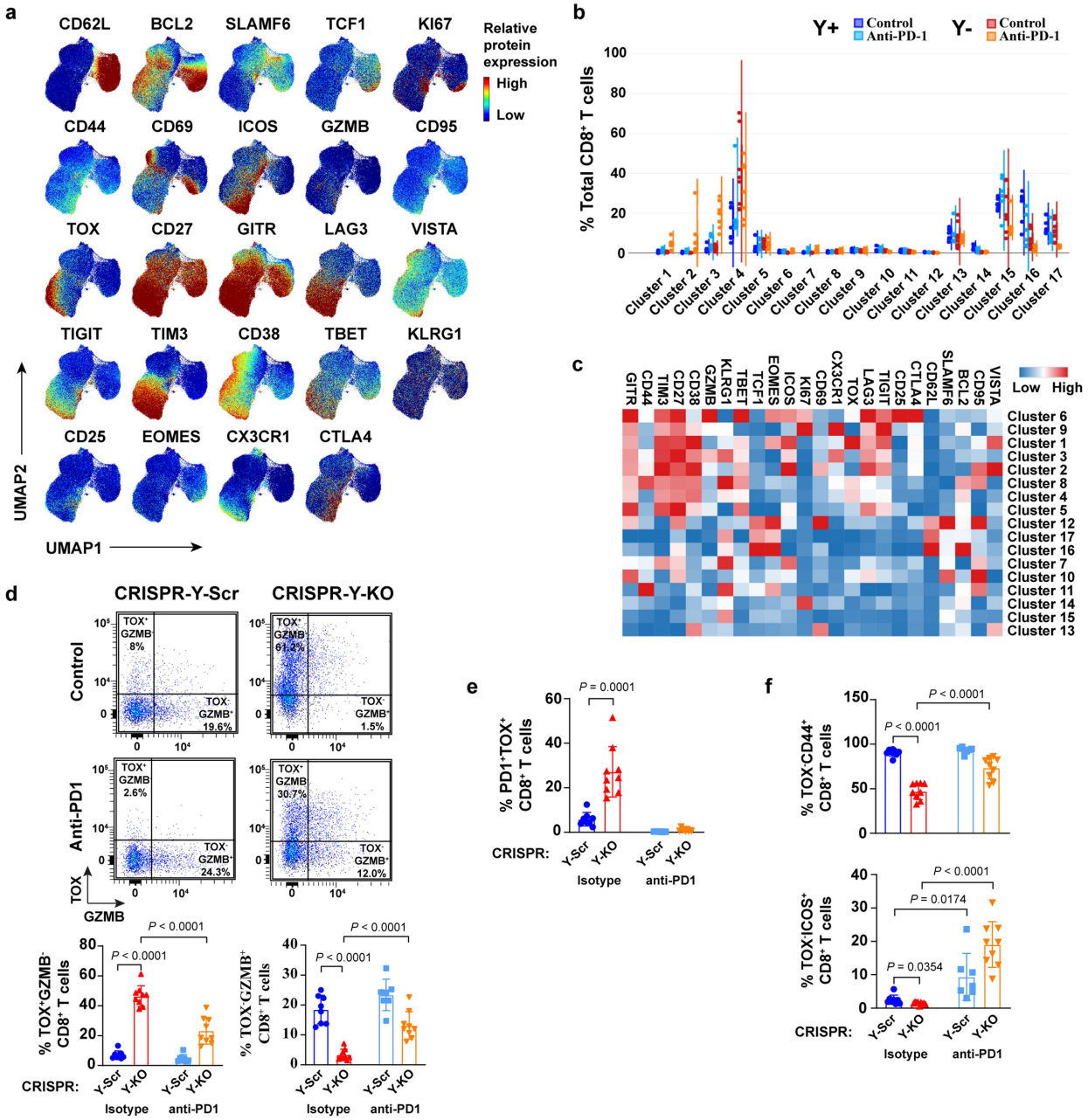

Extended Data Fig. 7 | Characterization of tumor-infiltrating CD8⁺ T cells after PD-1 pathway blockade. a–**c**, Relative spectral flow protein expression (**a**), sample-level violin plots per cluster (**b**), and heatmap of individual targets per cluster (**c**) after 200 µg anti-PD-1 or isotype control IgG treatments for 7 days using CD8⁺ T cells from Y+ and Y- MB49 tumors. **d**, Representative dot plots and percentages of TOX and/or GZMB-expressing CD8⁺ T cells from CRISPR-Y-Scr and CRISPR-Y-KO MB49 tumors grown in male WT mice after 200 µg anti-PD-1 or isotype control IgG treatments for 7 days. **e**–**f**, Percentage of PD1⁺TOX⁺ CD8⁺ T cells (**e**) and TOX⁻CD44⁺ (top panel) or TOX⁻ICOS⁺ (bottom panel) CD8⁺ T cells (**f**) from tumor samples described in **d**. See Fig. 5 for additional method details. Statistical significance was determined by two-sided unpaired *t*-test. Tests were conducted between isotype controls or between isotype controls and anti-PD1 treatment groups.

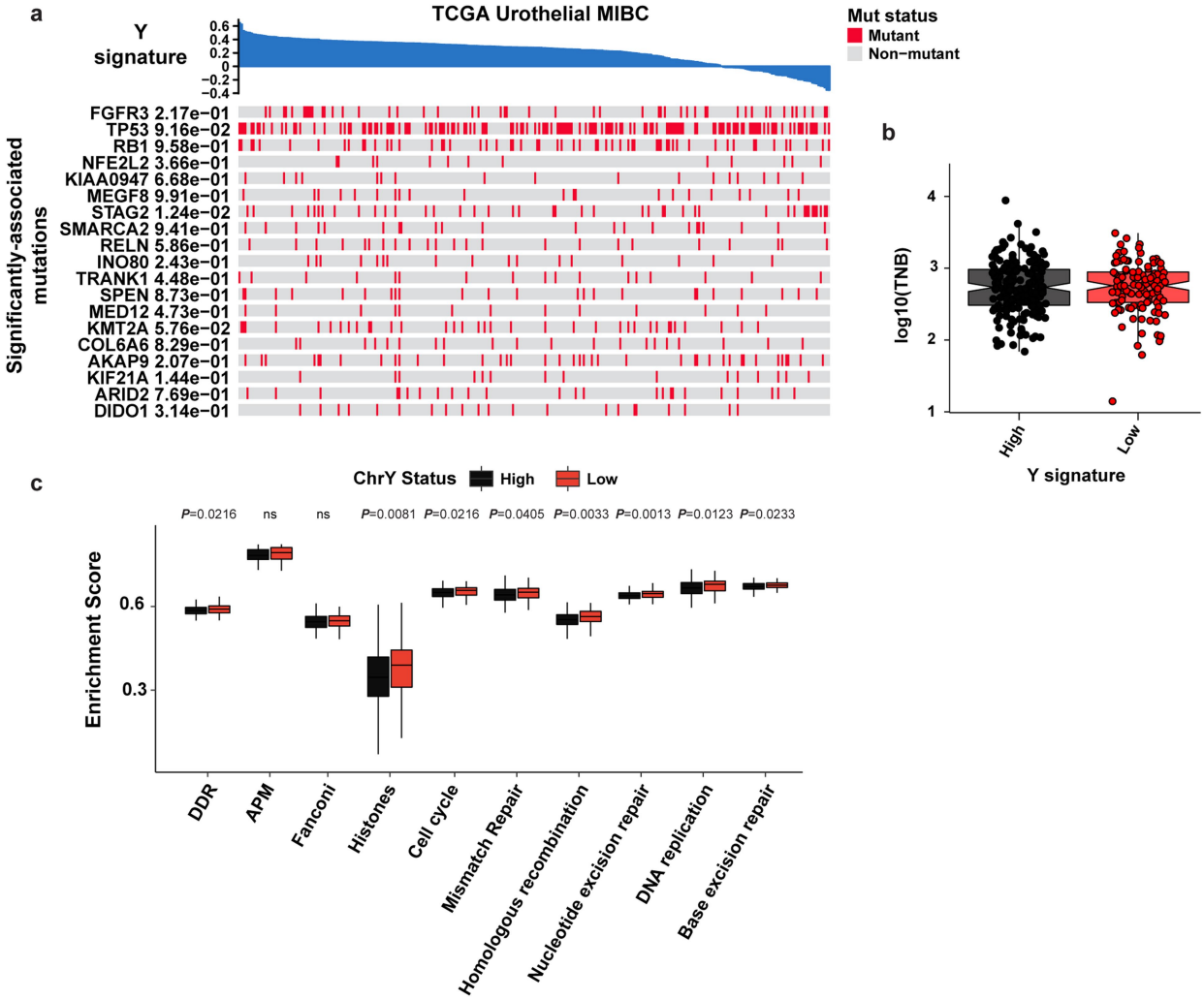

Extended Data Fig. 8 | DDR-related pathways in TCGA Y_{low} vs. Y_{high} BC. **a**, Heatmap of the indicated pathways and metadata from BC TCGA data. **b**–**c**, box plot of tumor neoantigen burden (TNB) per megabase ($P = 0.700$) (**b**), and associated pathway enrichment levels (**c**) from Y_{high} and Y_{low} tumors described in Fig. 1a. Statistical significance was determined by Wilcoxon test (Y_{low} n = 118 and Y_{high} n = 182). Boxplots represent the mean with first and third quartile data. Minimum and maximum datapoints are included.

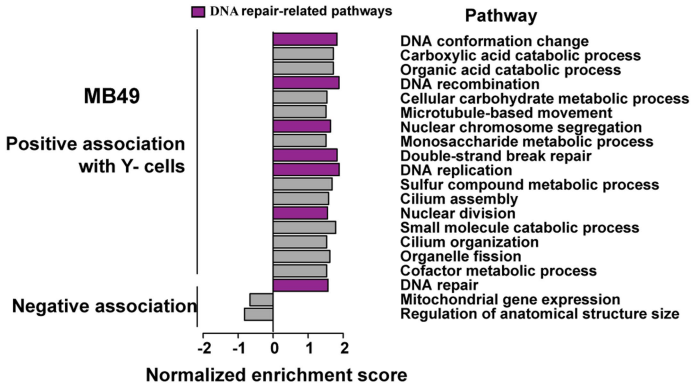

Extended Data Fig. 9 | Defective DDR pathway activation in Y- MB49 cells. Normalized enrichment scores of statistically significant GSEA GO pathways using DEGs from Y- vs. Y+ MB49 cell cultures. Purple color denotes DNA repair-related pathways enriched in Y- cells.

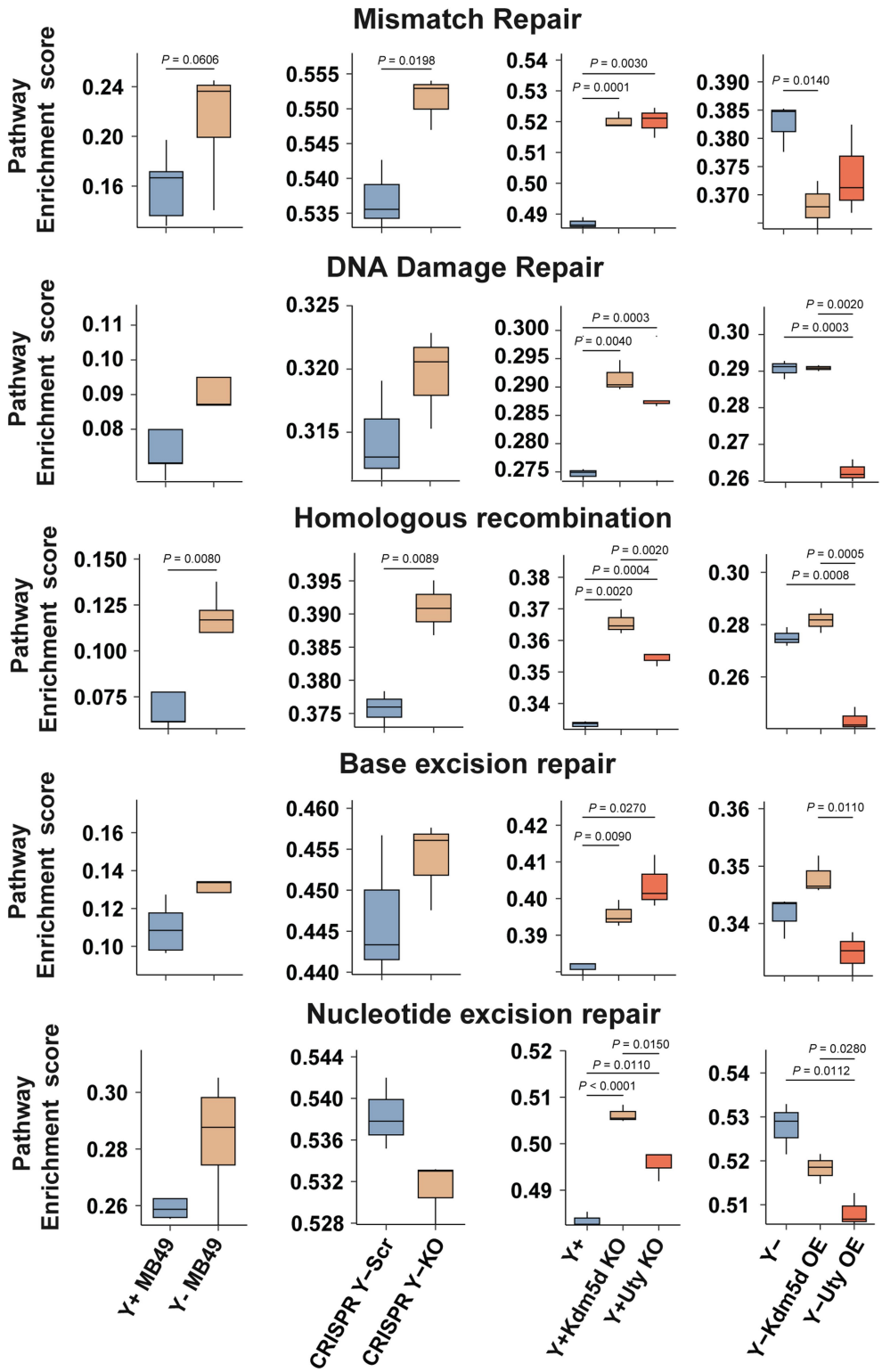

Extended Data Fig. 10 | Elevated genomic instability in LOY, *Uty* KO, and *Kdm5d* KO MB49 lines. Genome instability pathway enrichment scores using RNA-seq data from control and genetically modified MB49 cell lines (Y+ and Y- cells, n = 5 technical replicates. n = 3 for all other cell lines). Two-sided unpaired *t*-test. Boxplots represent the mean with first and third quartile data. Minimum and maximum datapoints are included.

nature portfolio

Corresponding author(s): Dan Theodorescu

Last updated by author(s): May 3, 2023

Reporting Summary

Nature Portfolio wishes to improve the reproducibility of the work that we publish. This form provides structure for consistency and transparency in reporting. For further information on Nature Portfolio policies, see our Editorial Policies and the Editorial Policy Checklist.

Statistics

For all statistical analyses, confirm that the following items are present in the figure legend, table legend, main text, or Methods section.

n/a	Confirmed
☐	☒ The exact sample size (*n*) for each experimental group/condition, given as a discrete number and unit of measurement
☐	☒ A statement on whether measurements were taken from distinct samples or whether the same sample was measured repeatedly
☐	☒ The statistical test(s) used AND whether they are one- or two-sided *Only common tests should be described solely by name; describe more complex techniques in the Methods section.*
☐	☒ A description of all covariates tested
☐	☒ A description of any assumptions or corrections, such as tests of normality and adjustment for multiple comparisons
☐	☒ A full description of the statistical parameters including central tendency (e.g. means) or other basic estimates (e.g. regression coefficient) AND variation (e.g. standard deviation) or associated estimates of uncertainty (e.g. confidence intervals)
☐	☒ For null hypothesis testing, the test statistic (e.g. *F*, *t*, *r*) with confidence intervals, effect sizes, degrees of freedom and *P* value noted *Give P values as exact values whenever suitable.*
☒	☐ For Bayesian analysis, information on the choice of priors and Markov chain Monte Carlo settings
☐	☒ For hierarchical and complex designs, identification of the appropriate level for tests and full reporting of outcomes
☒	☐ Estimates of effect sizes (e.g. Cohen's *d*, Pearson's *r*), indicating how they were calculated

Our web collection on statistics for biologists contains articles on many of the points above.

Software and code

Policy information about availability of computer code

Data collection	High Dimensional Flow cytometry (Cytek, Aurora). Imaging: Olympus BX43 Light microscope, Olympus DP26 Digital Camera. QuantStudio™ 6 Flex Real-Time PCR System. Plate reader (BioTeK). Nanostring GeoMx Digital Spatial Profiling (DSP) platform were used for immune profiling. Sequencing: Illumina HiSeq2500, Nextseq500, Novaseq 6000 (https://www.illumina.com/). Human data was downloaded directly from the "The Cancer Genome Atlas", Data from the IMvigor210 trial were obtained from the IMvigorCoreBiology R package, made freely available by the authors of the trial manuscript. For the snSeq analysis, data were downloaded from GEO (GSE169379,GSE171351). CODEX data were downloaded from https://figshare.com/s/4610a15363c8306dfa36, https://figshare.com/s/2005255a8b65de23109f https://figshare.com/s/1d8c7ed76d4b3222ada4.
Data analysis	GraphPad Prism 8.0, Microsoft Excel, ImageJ, GeoMx DSP analysis suite (GEOMX-0069), OMIQ cytometry analysis, Data Analysis was performed using R versions 4.1.2 or 4.2.3 and Python 3.9.4: ssGSEA, package GSEApy v0.10.1. scanpy v1.9.1. DESeq2 software version 1.26.0. MSigDB database. The microenvironment cell populations-counter (MCP counter). Kaplan-Meier survival analysis was performed using the survminer package in R software. NetMHCpan-3.0 algorithm.

For manuscripts utilizing custom algorithms or software that are central to the research but not yet described in published literature, software must be made available to editors and reviewers. We strongly encourage code deposition in a community repository (e.g. GitHub). See the Nature Portfolio guidelines for submitting code & software for further information.

Data

Policy information about availability of data

All manuscripts must include a data availability statement. This statement should provide the following information, where applicable:

- Accession codes, unique identifiers, or web links for publicly available datasets
- A description of any restrictions on data availability
- For clinical datasets or third party data, please ensure that the statement adheres to our policy

The authors declare that the data supporting the findings of this study are available within the paper, Extended Data files, Supplementary Information, Source data tables or will be available upon publication or on request. There is no restriction on data availability.

Human research participants

Policy information about studies involving human research participants and Sex and Gender in Research.

Reporting on sex and gender	*Use the terms sex (biological attribute) and gender (shaped by social and cultural circumstances) carefully in order to avoid confusing both terms. Indicate if findings apply to only one sex or gender; describe whether sex and gender were considered in study design whether sex and/or gender was determined based on self-reporting or assigned and methods used. Provide in the source data disaggregated sex and gender data where this information has been collected, and consent has been obtained for sharing of individual-level data; provide overall numbers in this Reporting Summary. Please state if this information has not been collected. Report sex- and gender-based analyses where performed, justify reasons for lack of sex- and gender-based analysis.*
Population characteristics	*Describe the covariate-relevant population characteristics of the human research participants (e.g. age, genotypic information, past and current diagnosis and treatment categories). If you filled out the behavioural & social sciences study design questions and have nothing to add here, write "See above."*
Recruitment	*Describe how participants were recruited. Outline any potential self-selection bias or other biases that may be present and how these are likely to impact results.*
Ethics oversight	*Identify the organization(s) that approved the study protocol.*

Note that full information on the approval of the study protocol must also be provided in the manuscript.

Field-specific reporting

Please select the one below that is the best fit for your research. If you are not sure, read the appropriate sections before making your selection.

☒ Life sciences ☐ Behavioural & social sciences ☐ Ecological, evolutionary & environmental sciences

For a reference copy of the document with all sections, see nature.com/documents/nr-reporting-summary-flat.pdf

Life sciences study design

All studies must disclose on these points even when the disclosure is negative.

Sample size	The sample size in each experimental group was determined based on a previously published studies of similar models (Tu et al., Science Advances 2019; 5(2).
Data exclusions	All samples that met adequate experimental conditions were included in the analysis. Samples that failed the Grubb's test for outliers in GraphPad 6.0 were excluded.
Replication	Experiments were successfully performed a minimum of two times and/or with sufficient animals per group to demonstrate statistical significance.
Randomization	Mice were randomized to treatment groups and blinded to researcher for the duration of the experiment. The same batch and number of cancer cells were injected per experiment, and all animals were housed under the same conditions.
Blinding	Investigators were blinded to group allocation during the experiment. All analysis was performed consistently during all studies and all tumor counts were performed by the same investigator.

Reporting for specific materials, systems and methods

We require information from authors about some types of materials, experimental systems and methods used in many studies. Here, indicate whether each material, system or method listed is relevant to your study. If you are not sure if a list item applies to your research, read the appropriate section before selecting a response.

Materials & experimental systems

n/a	Involved in the study
☐	☒ Antibodies
☐	☒ Eukaryotic cell lines
☒	☐ Palaeontology and archaeology
☐	☒ Animals and other organisms
☒	☐ Clinical data
☒	☐ Dual use research of concern

Methods

n/a	Involved in the study
☒	☐ ChIP-seq
☐	☒ Flow cytometry
☒	☐ MRI-based neuroimaging

Antibodies

Antibodies used

Antibodies used were for high-dimensional flow cytometry and included CD45 (BV510, Biolegend, 103138, dilution 1:400), CD3 (BUV737, BD Biosciences, 612771, dilution 1:200), CD8 (BUV496, BD Biosciences, 750024, dilution 1:400), CD4 (APC-Fire 810, Biolegend, 100480, dilution 1:400), CD11b (Alexa Fluor 532, eBioscience, 58-0112-82, dilution 1:800), NK1.1 (BV570, Biolegend, 108733, dilution 1:200), PD1 (FITC, eBioscience, 11-9985-82, dilution 1:200), TIM3 (BV711, Biolegend, 119727, dilution 1:200), SLAMF6 (APC, eBioscience, 17-1508-82, dilution 1:200), CD44 (BUV661, BD Biosciences, 741471, dilution 1:400), CD62L (BV421, Biolegend, 104436, dilution 1:400), LAG3 (BUV805, BD Biosciences, 748540, dilution 1:100), KLRG1 (Pacific Orange, eBioscience, 79-5893-82, dilution 1:200), VISTA (Super Bright 600, eBioscience, 63-1083-82, dilution 1:200), TIGIT (BV650, BD Biosciences, 744213, dilution 1:200), CX3CR1 (APC-Cy7, Biolegend, 149040, dilution 1:400), ICOS (Super Bright 436, eBioscience, 62-9949-82, dilution 1:400), CD27 (BUV563, BD Biosciences, 741275, dilution 1:400), CD38 (BV750, BD Biosciences, 747103, dilution 1:400), CD95 (BV480, BD Biosciences, 746755, dilution 1:200), CD25 (BB515, BD Biosciences, 564424, dilution 1:200), GITR (BUV615, BD Biosciences, 751532, dilution 1:800), CD69 (PE-Cy5, Biolegend, 104510, dilution 1:1000), FOXP3 (eFluor 450, eBioscience, 48-5773-82, dilution 1:800), TOX (PE, Miltenyi, 130-120-716, dilution 1:600), TCF1 (PE-Cy7, Cell Signaling, 90511s, dilution 1:600), CTLA4 (PE-DAZZLE 594, Biolegend, 106318, dilution 1:400), TBET (BV786, BD Biosciences, 564141, dilution 1:100), KI67 (BUV395, BD Biosciences, 564071, dilution 1:200), BCL2 (Alexa Fluor 647, Biolegend, 633510, dilution 1:200), EOMES (PerCP-eFluor 710, eBioscience, 46-4875-82, dilution 1:200), GZMB (AF700, Biolegend, 372222, dilution 1:200),F4/80(BUV395, BD Biosciences, 565614, 1:200), CD11c(BV750, Biolegend, 117357, 1:2000), MHCII (I-A/I-E)(BUV615, BD Biosciences, 751570, 1:1600), CD45R/B220(BV786, BD Biosciences, 563894, 1:600), Ly-6C(BV605, Biolegend, 128036, 1:2000), Ly-6G(Super Bright 436, Invitrogen, 62-9668-82, 1:400), CD103(BV711, BD Biosciences, 564320, 1:400), CD38(PE-cy7, Biolegend, 102718, 1:6400), TCR β(PE-cy5, Biolegend, 109210, 1:3000), CD64(APC, Invitrogen, 17-0641-82, 1:400), XCR1(PerCP-Cy5.5, Biolegend, 148208, 1:200), CD172a(PE-DAZZLE 594, Biolegend, 144016, 1:400), CD19(Spark NIR 685, Biolegend, 115568, 1:2000), CD24(BV480, BD Biosciences, 746709, 1:400), TCR γδ(BUV563, BD Biosciences, 749464, 1:800), PDL1(BV421, Biolegend, 124315, 1:400), CD206(APC-eFluor 780, Invitrogen, 47-2061-82, 1:5000), Arginase 1(Alexa Fluor 700, Invitrogen, 56-3697-82, 1:5000).

Validation

Pre-validated antibodies were purchased from well recognized vendors and were reported by other researchers. We based specificity on their provided description and data sheets.

Eukaryotic cell lines

Policy information about cell lines and Sex and Gender in Research

Cell line source(s)

The parental MB49 cell line was a gift from Dr. Marie Burdick, University of Virginia.

Authentication

Cell lines were authenticated by morphology and whole exome sequencing.

Mycoplasma contamination

All cell lines tested negative for mycoplasma contamination.

Commonly misidentified lines
(See ICLAC register)

N/A

Animals and other research organisms

Policy information about studies involving animals; ARRIVE guidelines recommended for reporting animal research, and Sex and Gender in Research

Laboratory animals

WT C57BL/6 and various syngeneic immune-deficient male mice were purchased from Taconic or the Jackson Laboratory and were received at 6 weeks old. Mice were allowed to acclimate for at least one week in sterile micro cages with constant temperature and humidity. Mice had free access to food and water.

Wild animals

Wild animals were not used in this study.

Reporting on sex

Indicate if findings apply to only one sex; describe whether sex was considered in study design, methods used for assigning sex. Provide data disaggregated for sex where this information has been collected in the source data as appropriate; provide overall numbers in this Reporting Summary. Please state if this information has not been collected. Report sex-based analyses where

	performed, justify reasons for lack of sex-based analysis.
Field-collected samples	Field-collected samples were not used in this study.
Ethics oversight	Mice were housed in specific-pathogen-free conditions and cared for in accordance with US National Institutes of Health guidelines, and all procedures were approved by Cedars-Sinai Medical Center and The Ohio State University Animal under Institutional Animal Care & Use Committee (IACUC) approved protocols.

Note that full information on the approval of the study protocol must also be provided in the manuscript.

Flow Cytometry

Plots

Confirm that:

☒ The axis labels state the marker and fluorochrome used (e.g. CD4-FITC).

☒ The axis scales are clearly visible. Include numbers along axes only for bottom left plot of group (a 'group' is an analysis of identical markers).

☒ All plots are contour plots with outliers or pseudocolor plots.

☒ A numerical value for number of cells or percentage (with statistics) is provided.

Methodology

Sample preparation	MB49 tumors were mechanically disrupted and subjected to digestion via 1 mg/mL Collagenase D (Roche) for 30 min at 37°C with agitation. Two percent bovine serum albumin in ice-cold PBS was used to inactivate enzymatic activity. Red blood cell lysis buffer (BioLegend) was used before cells were passed through 70 µm filters to generate single cell suspensions. Cells were then stained at 4°C with LIVE/DEAD blue fixable viability dye for 15 minutes (Invitrogen), followed by extracellular surface markers and FcR block concurrently for 40 minutes.
Instrument	High Dimensional Flow cytometry (Cytek, Aurora)
Software	Analyses were performed the using OMIQ flow cytometry analysis platform.
Cell population abundance	Cells were gated as described below using the OMIQ flow cytometry analysis platform. Flow panels were optimized where there were clear negative and positive marker separations. After gating for live, CD45+ singlets, or live, CD8+ T cells, a similar cell number was selected from each tumor (10,000 cells/sample for all immune cell analyses and 4,000 cells/sample for CD8+ T cell analyses). Given the high dimensionality of the spectral flow, OMIQ was used to perform dimensional reduction with Uniform Manifold Approximation and Projection (UMAP), thereby identifying specific cell populations whose abundance could be statistically evaluated between model or treatment conditions.
Gating strategy	Gating was performed according to standard gating strategies. First, we distinguished cell populations based on their forward and side scatter to select those of the appropriate size and granularity. Doublets were excluded by assessing cells outside of the diagonal axis when assessing FSC height versus area. For samples used to assess various immune cell populations between tumor conditions, we next gated for live, CD45+ cells. These cells were negative for LiveDead blue staining and positive for CD45 expression. For those samples where we were assessing CD8+ T cell populations, additional gating was carried out after selecting for those that were live, CD45+. Cell populations were then selected for negativity for both CD11b to negatively select out myeloid and NK cell population. We next selected cells that were positive for CD3. Final gating was on cells that were CD8 positive and CD4 negative. Additional markers such as F4/80 were used to identify macrophage cell populations, along with CD11b.

☒ Tick this box to confirm that a figure exemplifying the gating strategy is provided in the Supplementary Information.